AFRL-AFOSR-VA-TR-2017-0052

Catalysts for Lightweight Solar Fuels Generation

Daniel Nocera
HARVARD COLLEGE PRESIDENT & FELLOWS OF
1350 MASS AVE STE 600
CAMBRIDGE, MA 02138-3846

03/20/2017
Final Report

Air Force Research Laboratory
AF Office Of Scientific Research (AFOSR)/RTB2

REPORT DOCUMENTATION PAGE

Form Approved
OMB No. 0704-0188

PLEASE DO NOT RETURN YOUR FORM TO THE ABOVE ORGANIZATION.

1. REPORT DATE *(DD-MM-YYYY)*	2. REPORT TYPE	3. DATES COVERED *(From - To)*
10-03-2017	Final Report	01-02-2013 to 31-01-2017

4. TITLE AND SUBTITLE
Catalysts for Lightweight Solar Fuels Generation

5a. CONTRACT NUMBER

5b. GRANT NUMBER
FA9550–13–1–00289

5c. PROGRAM ELEMENT NUMBER

6. AUTHOR(S)
Nocera, Daniel G.

5d. PROJECT NUMBER

5e. TASK NUMBER

5f. WORK UNIT NUMBER

7. PERFORMING ORGANIZATION NAME(S) AND ADDRESS(ES)
President and Fellows of Harvard College
1033 Massachusetts Avenue, 5th Floor
Cambridge, MA 02138

8. PERFORMING ORGANIZATION REPORT NUMBER
NA

9. SPONSORING/MONITORING AGENCY NAME(S) AND ADDRESS(ES)
Air Force Office of Scientific Research
875 North Randolph Street 4027
Arlington VA 22203

10. SPONSOR/MONITOR'S ACRONYM(S)
NA

11. SPONSOR/MONITOR'S REPORT NUMBER(S)
NA

12. DISTRIBUTION/AVAILABILITY STATEMENT
Distribution A - Approved for Public Release

13. SUPPLEMENTARY NOTES

14. ABSTRACT

The artificial leaf has been created to provide a simple mechanism for the storage of solar energy in the form of the chemical fuels of hydrogen and oxygen, produced from solar water splitting. The artificial leaf comprises a single crystalline Si coated with a NiMoZn or Co-P alloy as the hydrogen evolution catalyst and cobalt phosphate (CoPi) or nickel borate (NiBi) as the oxygen evolution catalyst. Modeling this buried junction architecture provided a rational framework for the design and construction of devices with solar-to-hydrogen efficiencies greater than 10%. The concept of solar fuels was advanced by coupling the functional componentry of the artificial leaf with the hydrogen-oxidizing bacteria, Ralstonia eutropha. In this body of work, R. eutropha is used to efficiently convert carbon dioxide, along with hydrogen produced from water splitting catalysts of the artificial leaf, into biomass and fusel alcohols. In this integrated setup, equivalent solar-to-biomass yields of up to 10.2% and solar-to-liquid fuel yields of 5-7% have been achieved. These yields greatly exceed natural photosynthetic systems of crops (1%) and microalgae (3%). The work provides a distributed method to store solar energy in the form of fuels.

15. SUBJECT TERMS
distributed energy, off-grid, solar, fuels, hydrogen

16. SECURITY CLASSIFICATION OF:			17. LIMITATION OF ABSTRACT	18. NUMBER OF PAGES	19a. NAME OF RESPONSIBLE PERSON
a. REPORT	b. ABSTRACT	c. THIS PAGE			Adair L. Swain
U	U	U	UU		19b. TELEPHONE NUMBER *(Include area code)* 617-496-4598

Reset

INSTRUCTIONS FOR COMPLETING SF 298

1. REPORT DATE. Full publication date, including day, month, if available. Must cite at least the year and be Year 2000 compliant, e.g. 30-06-1998; xx-06-1998; xx-xx-1998.

2. REPORT TYPE. State the type of report, such as final, technical, interim, memorandum, master's thesis, progress, quarterly, research, special, group study, etc.

3. DATES COVERED. Indicate the time during which the work was performed and the report was written, e.g., Jun 1997 - Jun 1998; 1-10 Jun 1996; May - Nov 1998; Nov 1998.

4. TITLE. Enter title and subtitle with volume number and part number, if applicable. On classified documents, enter the title classification in parentheses.

5a. CONTRACT NUMBER. Enter all contract numbers as they appear in the report, e.g. F33615-86-C-5169.

5b. GRANT NUMBER. Enter all grant numbers as they appear in the report, e.g. AFOSR-82-1234.

5c. PROGRAM ELEMENT NUMBER. Enter all program element numbers as they appear in the report, e.g. 61101A.

5d. PROJECT NUMBER. Enter all project numbers as they appear in the report, e.g. 1F665702D1257; ILIR.

5e. TASK NUMBER. Enter all task numbers as they appear in the report, e.g. 05; RF0330201; T4112.

5f. WORK UNIT NUMBER. Enter all work unit numbers as they appear in the report, e.g. 001; AFAPL30480105.

6. AUTHOR(S). Enter name(s) of person(s) responsible for writing the report, performing the research, or credited with the content of the report. The form of entry is the last name, first name, middle initial, and additional qualifiers separated by commas, e.g. Smith, Richard, J, Jr.

7. PERFORMING ORGANIZATION NAME(S) AND ADDRESS(ES). Self-explanatory.

8. PERFORMING ORGANIZATION REPORT NUMBER. Enter all unique alphanumeric report numbers assigned by the performing organization, e.g. BRL-1234; AFWL-TR-85-4017-Vol-21-PT-2.

9. SPONSORING/MONITORING AGENCY NAME(S) AND ADDRESS(ES). Enter the name and address of the organization(s) financially responsible for and monitoring the work.

10. SPONSOR/MONITOR'S ACRONYM(S). Enter, if available, e.g. BRL, ARDEC, NADC.

11. SPONSOR/MONITOR'S REPORT NUMBER(S). Enter report number as assigned by the sponsoring/ monitoring agency, if available, e.g. BRL-TR-829; -215.

12. DISTRIBUTION/AVAILABILITY STATEMENT. Use agency-mandated availability statements to indicate the public availability or distribution limitations of the report. If additional limitations/ restrictions or special markings are indicated, follow agency authorization procedures, e.g. RD/FRD, PROPIN, ITAR, etc. Include copyright information.

13. SUPPLEMENTARY NOTES. Enter information not included elsewhere such as: prepared in cooperation with; translation of; report supersedes; old edition number, etc.

14. ABSTRACT. A brief (approximately 200 words) factual summary of the most significant information.

15. SUBJECT TERMS. Key words or phrases identifying major concepts in the report.

16. SECURITY CLASSIFICATION. Enter security classification in accordance with security classification regulations, e.g. U, C, S, etc. If this form contains classified information, stamp classification level on the top and bottom of this page.

17. LIMITATION OF ABSTRACT. This block must be completed to assign a distribution limitation to the abstract. Enter UU (Unclassified Unlimited) or SAR (Same as Report). An entry in this block is necessary if the abstract is to be limited.

AFOSR Final Performance Report

Title:	Catalysts for Lightweight Solar Fuels Generation
Grant. Number:	FA9550–13–1–00289
Program Manager:	Dr. Patrick O. Bradshaw Air Force Office of Scientific Research 875 North Randolph Street 4027 Arlington VA 22203 Email: patrick.bradshaw.3@us.af.mil
Principal Investigator:	Daniel G. Nocera Department of Chemistry and Chemical Biology Harvard University 12 Oxford Street Cambridge, MA 02138 Email: dnocera@fas.harvard.edu

Summary

The artificial leaf was created to provide a simple mechanism for the storage of solar energy in the form of the chemical fuels of hydrogen and oxygen, produced from solar water splitting. The artificial leaf comprises a single crystalline Si coated with a NiMoZn or Co-P alloy as the hydrogen evolution catalyst and cobalt phosphate (CoP_i) or nickel borate (NiB_i) as the oxygen evolution catalyst. Modeling this buried junction architecture provided a rational framework for the design and construction of devices with solar-to-hydrogen efficiencies greater than 10%. The concept of solar fuels was advanced by coupling the functional componentry of the artificial leaf with the H_2-oxidizing bacteria, *Ralstonia eutropha*. In this body of work, *R. eutropha* is used to efficiently convert CO_2, along with H_2 produced from water splitting catalysts of the artificial leaf, into biomass and fusel alcohols. In this integrated setup, equivalent solar-to-biomass yields of up to 10.2% and solar-to-liquid fuel (e.g., fusel alcohols) yields of 5-7% have been achieved. These yields greatly exceed natural photosynthetic systems of crops (1%) and microalgae (3%). This scalable system scrubs a CO_2 equivalent of about 230,000 liters of air per kWh of electricity. The work provides a distributed method to store solar energy in the form of fuels.

1 The Artificial Leaf

The artificial leaf is a buried junction device. In the artificial leaf, the solar input generates electron-hole pairs across the internal electric field of a semiconductor junction and they are then coupled to the water-splitting catalysts through ohmic contacts. The catalysts are directly deposited on the conductive coatings that sandwich the photovoltaic (PV) semiconducting material. Specifically, a Si-buried junction coated with transparent conducting oxides (TCOs) was overlaid with self-healing catalysts that self-assemble upon oxidation of Co^{2+}, Ni^{2+} and Mn^{2+} ions in the presence of phosphate (P_i) or borate (B_i) electrolytes. A goal during the project period was to optimize the performance of the artificial leaf by (i) determining the ideal TCO, (ii) providing a mathematical model for describing device performance and (iii) using this model to design an artificial leaf with a high solar-to-hydrogen efficiency.

1.1 Interfaces for the Artificial Leaf

The coupling of water-splitting catalysts to silicon photovoltaics enables direct solar-to-fuels conversion. Critical to the performance of such devices is the use of interfaces to protect silicon on the p-side of the buried junction from corrosion attendant to the oxygen evolving reaction (OER) and at the same time to provide ohmic contact between the buried Si junction and the mobilized OER catalyst. A highly efficient device requires minimal losses associated with bulk and interfacial carrier transport. A controlled study was undertaken to examine the performance of the artificial leaf as it related to different interfaces and different OER catalysts (CoB_i, NiB_i and NiFeO). The goal of the study was to replace the original transparent conducting oxide (TCO), indium-tin=oxide (ITO), with less expensive and more earth–abundant material. We determined that fluorine-doped–tin–oxide (FTO) is well-suited as an interface for the operation of the artificial leaf under neutral aqueous conditions.

The different Tafel slopes shown in Figure 1 depend both on catalytic activity and ohmic resistances arising primarily between the Si | catalyst interface We examined the anode activity of a variety of catalyst-protective coating combinations on the Si buried junction. For a given OER catalyst (e.g., CoB_i), the trend is the same. The Tafel slope for a FTO-coated electrode is lower

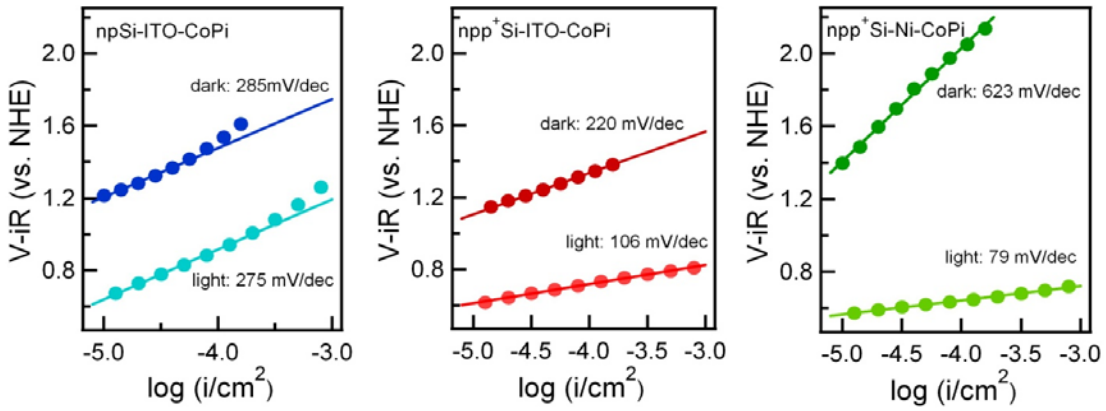

Figure 1 | Tafel data for *np*-Si-ITO-CoP_i (blue data), *npp*$^+$-Si-ITO-CoP_i (red data), and *npp*$^+$-Si-Ni-CoP_i (green data) in dark and under illumination with AM 1.5 light.

than that of an ITO; Ni-coated electrodes are also good conductors but they exhibit high variability. We believe that the variance of the Ni interface arises from oxidation of the Ni film to NiO. For this reason, FTO is a preferred coating as it avoids the use of rare elements (e.g., indium) and is also able to form highly conductive and reproducible films as prepared by a variety of deposition techniques.

1.2 Modeling the Artificial Leaf

Realization of a high solar-to-fuels efficiency (SFE) in the artificial leaf depends on matching the power output of the PV element with the power consumption of the OER catalyst. More specifically, the electrochemical load for water splitting (defined by the Tafel behavior of the catalysts and the cell resistances) should intersect the i-V curve of the solar cell at its maximum power point for maximal SFE to be realized. In the case of the artificial leaf, the catalysis and PV power curves may be adjusted independently, which is a virtue of a buried junction device.

In the artificial leaf, the operating current density is given by the intersection of the i-V curve for the PV and the i-V curve (i.e., Tafel curve) representing the electrochemical load for water splitting. This operating current density multiplied by the thermodynamic potential of water splitting (1.23 V) defines the power stored in water splitting, and the ratio of this power to the incident power of the solar flux, 100 mW/cm^2, defines the SFE. Figure 2 shows the results of modelling the idealized PV behavior of a triple junction amorphous Si(a–Si) | nanocrystalline Si(nc–Si) | nanocrystalline Si(nc–Si) triple junction cell stack possessing V_{oc} = 1.94 V and j_{sc} = 8.96 mA cm^{-2}, and a hypothetical multi-junction cell with a V_{oc} = 2.13 V and j_{sc} = 8.15 mA cm^{-2}. The idealized cells exhibit a power conversion efficiency of 16%, but display dramatically different SFEs when paired with the various OER catalysts. For the cell possessing the lower V_{oc}, the electrochemical load curves for water splitting using NiB_i, and CoB_i intersect the i-V curve of the PV at 1.85 and 1.89 V, respectively, which is beyond the maximum power point (V_{mp} = 1.83 V) of the PV. As the PV current density declines sharply beyond V_{mp}, an artificial leaf utilizing CoB_i is expected to exhibit a lower hydrogen production current density (7.6 mA cm^{-2}) than one utilizing NiB_i (8.7 mA cm^{-2}). Water splitting stores 1.23 V and, thus, these current densities translate to SFEs = 9.3% and 10.7% for CoB_i and NiB_i, respectively. The artificial leaf becomes even more insensitive to OER catalytic activity if the V_{oc} of the PV is increased (Figure 2). For the higher V_{oc} cell, all of the catalysts exhibit SFE = 10.0%, highlighting the fact that good catalyst

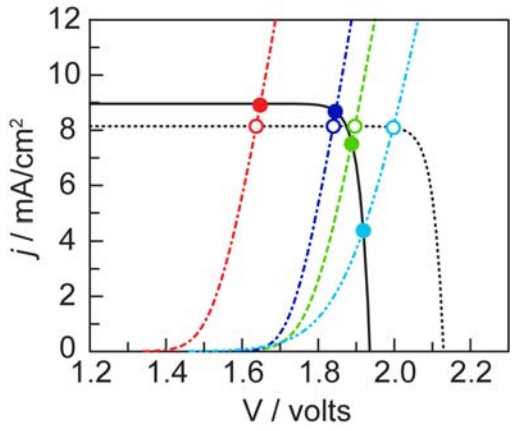

Figure 2 | Electrochemical load of water splitting utilizing CoB_i (— —), NiB_i (▪ — ▪), RuO_2 (— — ▪), and $LaMnO_3$ (▪ ▪ —) oxygen evolution catalysts and the i–V curve of an idealized model of an a–Si|nc–Si|nc–Si triple junction photovoltaic displaying V_{oc} = 1.94 V, j_{sc} = 8.96 mA cm^{-2} (—) and an idealized hypothetical cell possessing V_{oc} = 2.13 V, j_{sc} = 8.15 mA cm^{-2} (— —). Open circles indicate operating current densities for the high V_{oc} cell and correspond to 10% SFE for all catalysts. Close circles indicate operating current densities for the low V_{oc} cell for which SFE is sensitive to catalyst performance.

performance and high SFE is only mandated if a suitable PV with a V_{mp} matched to the electrochemical load can be designed near the thermodynamic potential of water splitting.

These results indicated that a key determinant of high SFE for artificial leaves is the OER kinetic profile. In particular, thin NiB_i catalyst films exhibit a 29 mV/decade Tafel slope as compared to a 52 mV/decade slopes observed for CoB_i under similar electrolyte conditions. The disparate kinetics of CoB_i and NiB_i translate into improved SFE of an artificial leaf utilizing the latter, suggesting that NiB_i is particularly well-suited to direct solar-to-fuels generation. These results suggested that SFEs = 10% were easily within reach if CoB_i and NiB_i catalysts are integrated with PV cells operating at 15% efficiency.

Modelling a second architecture showed that the power output of a series-connected string of single bandgap solar cells to OER catalysts could lead to very high solar-to-fuel efficiencies. Figure 3 illustrates a PV-EC utilizing a PV, an electrochemical system (made up of appropriate electrodes, catalysts, and electrolyte solution), and a coupling system. The purpose of the coupling system is to match the electrical output (current and voltage) of the PV device to the electrical input to the water splitting process. Given this arrangement, the steady-state efficiency η_{SF} with which solar power is transferred to chemical fuels is given by,

$$\eta_{SF} = \eta_{pv} \times \eta_{ec} \times \eta_{c}, \tag{1}$$

where η_{pv}, η_{ec} and η_{c} are the efficiencies of the PV device, EC process, and coupling arrangement, respectively. Solving for these three efficiencies showed that the direct electrical connection of a PV power source to an OER reaction as,

$$\eta = \frac{FF \times V_{oc} \times J_{sc}}{P_{sun}} \times \frac{\mu_{th}}{V_{op}} \times \frac{V_{op} \times J_{op}}{FF \times V_{oc} \times J_{sc}} = \frac{\mu_{th} \times J_{op}}{P_{sun}}. \tag{2}$$

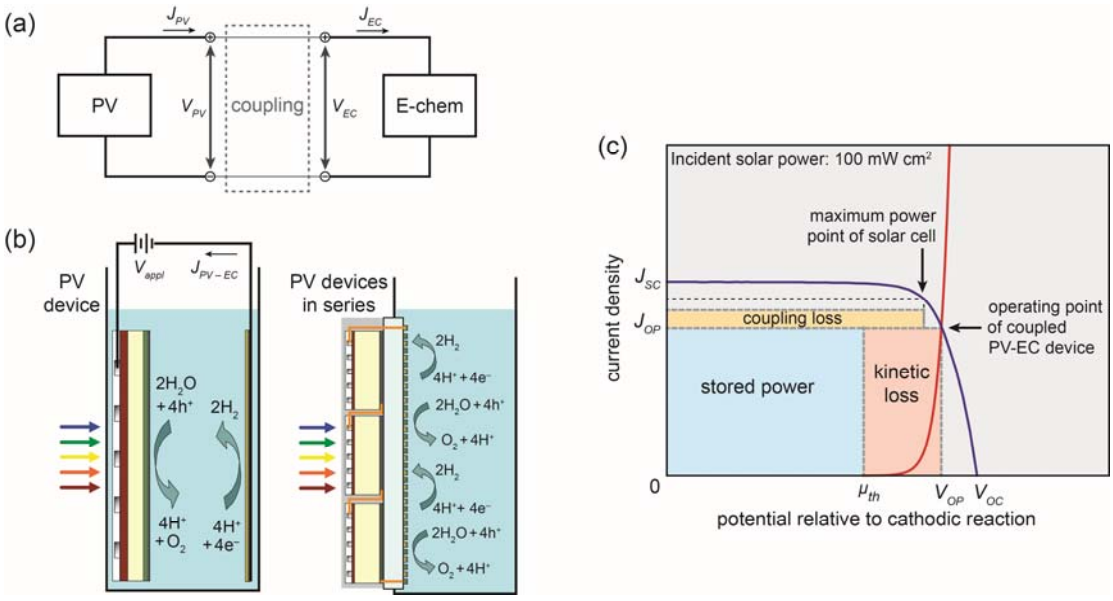

Figure 3 | (a) Block diagram of the arrangement for providing power to an electrochemical cell (EC) using a photovoltaic (PV) device via direct coupling, as well as (b) two examples of the experimental setup for direct coupling. An arrangement is shown that could minimize solution resistance by using interdigitated contacts. (c) The generalized current density-voltage (i-V) diagram of a directly coupled PV-EC device graphically identifies the power flows in the coupled system relative to total incident solar power. The plot represents a maximally efficient solar cell ($\eta_{\mathrm{pv}} = 30.8\%$) with open circuit voltage V_{oc} and short circuit current density J_{sc}; total plot area is scaled to incident solar power (100 mW cm^{-2}). The PV-EC system operates at the intersection of the current-voltage curves. At the operating current density J_{op}, power $J_{\mathrm{op}}V_{\mathrm{op}}$ is dissipated while energy is stored at a rate of $J_{\mathrm{op}}\mu_{th}$ (where μ_{th} is the thermodynamic potential of the reaction). The difference represents kinetic losses due to the overpotential. Coupling losses are defined as the difference between the maximum power output of the solar cell and the power dissipated in the electrochemistry. These losses are represented in region $J > J_{\mathrm{op}}$, although they are not dissipated at a single current or voltage.

In Figure 3c, these efficiency terms are summarized graphically. This equation may be used to determine scenarios for different numbers of cells connected in series (Figure 4). For single-absorber solar cells to generate a voltage sufficient to drive a reaction, several cells may have to be wired in series. As an outstanding Si solar cell produces a maximum voltage of about 700 mV, at least two cells, wired in series, are required to drive the water-splitting reaction ($\mu_{\mathrm{th}} = 1.23$ V). If an excess of cells is added in series, the operating point of the coupled PV-EC system would fall far from the maximum power point of the cell (Figure 4b: e.g., the intersection of the $R_{\mathrm{sol}} = 0$ electrochemical curve with the 3- and 4-cell curves).

Using this steady-state equivalent circuit analysis, the results suggested that SFEs = 10% were shown to be easily within reach if CoB_i and NiB_i catalysts were integrated with PV cells operating at 15% efficiency. We thus set out to construct a cell based on this analysis.

1.3 A >10% Artificial Leaf

Figure 5 shows a schematic of the coupled PV-EC device utilizing a c-Si PV module, NiB_i as the OER catalyst and NiMoZn as the HER catalyst. As shown by our modelling, the operating point for a PV-EC device is indicated graphically as the intersection point of the independently measured i-V curves for the PV and EC for water splitting. Figure 5C shows the i-V curve for mini-modules constructed from either 3- or 4 -single junction c-Si solar cells connected in series. Considering a PV-EC device based on commercially available single junction-Si solar cells and the Tafel

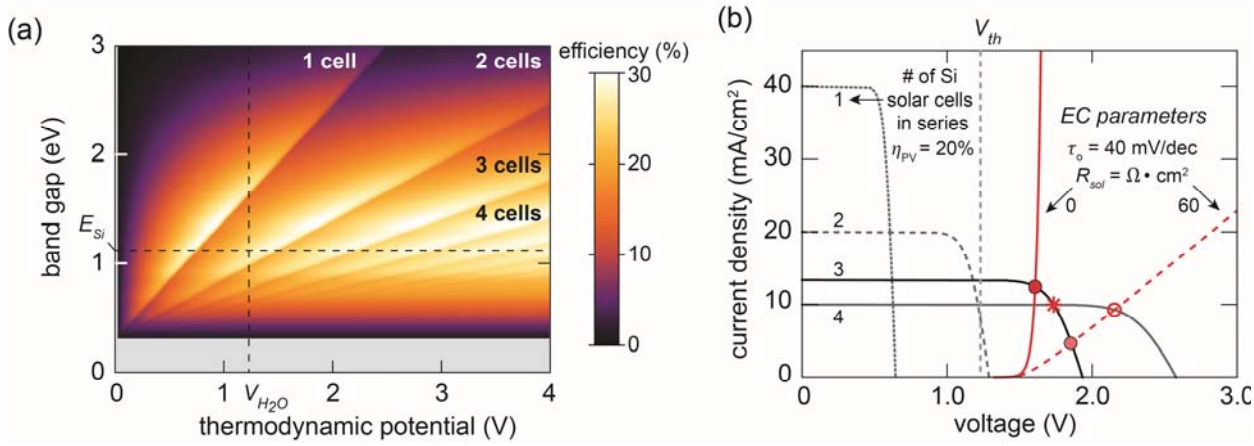

Figure 4 | (a) A density plot of the efficiency of utilizing the output power of ideal solar cell materials, characterized by band gap E_g, to produce stored chemical energy via reversible electrochemical (EC) reactions defined by a thermodynamic reaction potentials μ_{th}. Because only single-bandgap solar cell materials are considered, EC reactions with μ_{th} larger than the operating voltages of the solar cells (~$0.75 \times E_g/q$, where q is the fundamental charge) require multiple cells in series. The plot is separated by areas of rapidly changing efficiency into regions defined by the number of solar cells required for efficient coupling. The maximum theoretical solar-to-fuels efficiency is 30.8% (for $E_g = 1.38$ eV); for Si, the ideal SFE via water-splitting is 26.9%. (b) Current-voltage plot indicating the impact of electrochemical parameters on the coupling efficiency as well as the number of to realistic Si solar cells ($\eta_{th} = 20\%$) required for efficient coupling.

behavior of the catalysts, a 10% or higher SFE can be achieved using three single-junction c-Si devices series connected in a mini-module with a PV efficiency of 15% or higher (red dashed curve Figure 5C). However, resistive losses were not negligible and our modeling is Section 1.2 indicated that using a 4-cell c-Si module would overcome of resistive losses on SFE.

Figure 6A showed the measured J_{OP} of the device attained a SFE of 10.2% with an initial current density of 8.35 mA cm^{-2}. During the first few minutes of illumination J_{OP} decreased to a steady-state value of 7.8 mA cm^{-2}. The initial decline in J_{OP} was consistent with heating of the PV-module under illumination causing a decrease in solar cell voltage, which shifted the maximum power point toward the origin. In line with PV module heating, turning the lamp off for 5 min and then turning it back on causes the SFE to recover to 10.2% (Figure 6A). Additionally, the chopped illumination demonstrates the reproducibility in measuring J_{OP}. The operational stability of the coupled PV-EC system (Figure 6B) showed no decline in J_{OP} for over a week of operation in 0.5 M KB_i pH 9.2 solution. These results demonstrated that an SFE efficiency of 10% can be achieved utilizing non-precious materials and c-Si.

2 The Bionic Leaf

We have coupled the functional componentry of the artificial leaf with the H_2-oxidizing *Ralstonia eutropha* (Figure 7). This hybrid inorganic | biological construct is powered by H_2 produced from the catalysts of the artificial leaf. The bio-engineered bacterium converts carbon dioxide, along with H_2 into biomass and liquid fuels, thus closing an entire artificial photosynthetic cycle. The initial construct achieved solar-to-biomass efficiencies of 1.6% and solar-to-fuel efficiencies of 0.6%. With a redesign of the catalysts, a solar-to-biomass efficiency of 10.2% and a solar-to-fuel efficiency of 7.2% was achieved, greatly exceeding the 1% yield of natural photosynthesis.

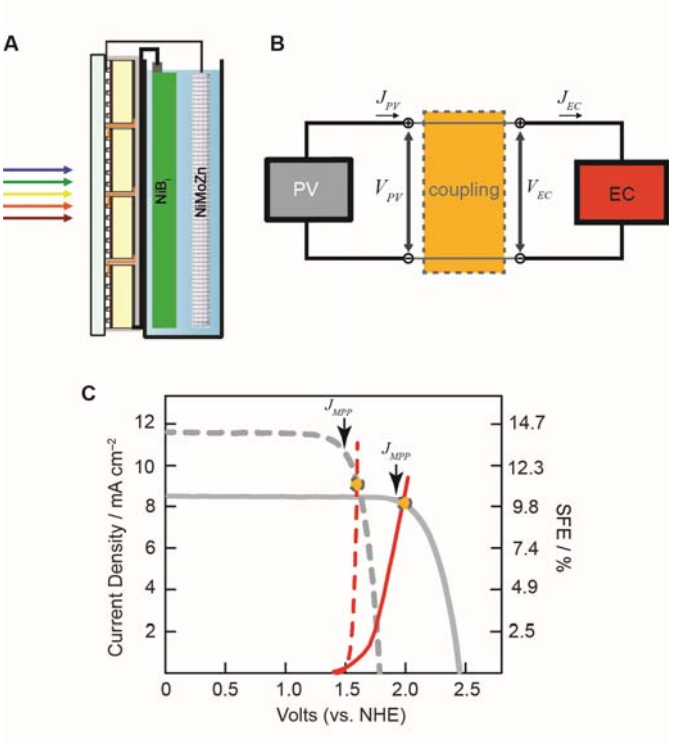

Figure 5 | A Schematic of the experimental setup and electrode geometry for the PV-EC device **B** Block diagram for an electrochemical load driven by a PV device. The direct electrical connection in which the two half-reactions occur on surfaces equipotential with the terminals of a solar cell describes both wired and wireless water-splitting and constrains the currents and voltages of the PV device and the EC system to be identical. **C** i-V curves of the individually measured PV and EC components making up the PV-EC device. The grey curves represent the i-V curve for the PV modules composed of either three (dashed) or four (solid) single junction c-Si solar cells measured under AM 1.5 illumination. The red dashed curve shows the ideal i-V curve obtained for NiB_i and NiMoZn catalysts based on previously reported Tafel analysis. The solid red curve curves show the J-V curve of the NiB_i and NiMoZn electrodes measured in a 2-electrode experiment (0.5 M KB_i / 0.5 M K_2SO_4, pH 9.2). The point of intersection represents the JOP and the SFE of the coupled system.

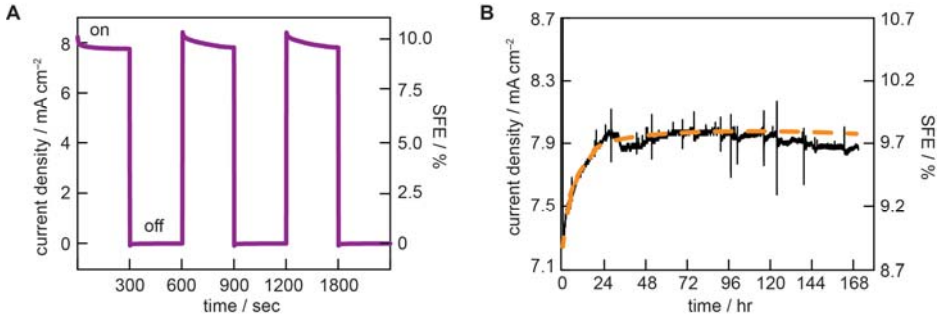

Figure 6 | A Current under chopped illumination representing J_{OP} for the PV-EC device (0.5 M KB_i / 0.5 M K_2SO_4, pH 9.2). The chopped illumination illustrates the recovery in SFE and illustrates the reproducibility in measuring J_{OP}. **B** J_{OP} measured for over 7 days of operation showing no decrease in SFE over operation time. Spikes J_{OP} are due to addition of solution to maintain the solution level and pH. The orange dashed line is a smoothed curve of the data.

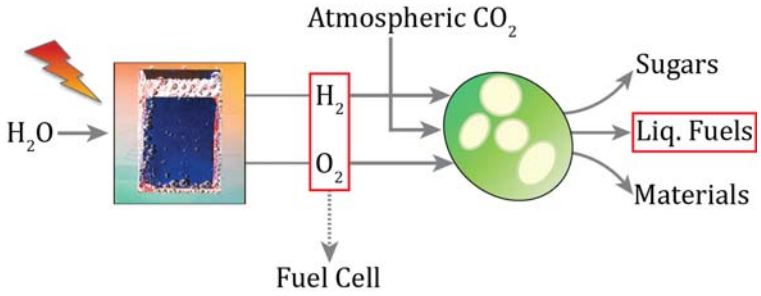

Figure 7 | Interfacing the water splitting competence of the artificial leaf with recent advances in synthetic biology makes the cost effective, renewable generation of an infrastructure compatible fuel.

2.1 Bionic Leaf v1.0

A scalable, integrated bioelectrochemical system was developed in which the bacterium *R. eutropha* is used to efficiently convert CO_2, along with H_2 produced from water splitting, into biomass and fusel alcohols. A schematic of the system and the cell configuration employed for the bioelectrochemical experiments is shown in Figure 8. *R. eutropha* was cultured in the cell using a CoP_i anode and either NiMoZn electrodeposited on stainless steel 304 mesh (SS) or plain SS mesh as a cathode. These electrodes furnished oxygen and hydrogen respectively, which was the sole source of biological reducing equivalents.

The potential E_{cell} required for water splitting current is in excess of 2 mA/cm^2 between 2.0 and 2.3 V, which is higher than the potentials needed for the CoP_i | NiMoZn system in buffer solutions for two reasons. First, the solution resistivity of the growth medium was measured to be significantly higher (Ω_{soln} = 62.4 ohms) than normal water splitting conditions owing to a relatively overall low salt concentration. Second, in the presence of the growth medium, the OER (η_{OER}) and HER (η_{HER}) overpotentials are higher than in buffered solutions. The relative contributions of the CoP_i anode, NiMoZn cathode (vide infra) and solution resistivity to the overall cell is schematically summarized in Figure 8B.

Growth at 2.3 V is achievable (Figure 9A). We note that CoP_i | NiMoZn electrodes and *R. eutropha* were reciprocally compatible under applied potentials: CoP_i and NiMoZn electrodes permitted biological growth and conversely, biological growth did not oppose long-term catalyst function.

As established by the spot assays from its cathodic and anodic chambers (Figure 10A), toxicity occurred exclusively at the cathode for cell potentials poised at a significant water-splitting underpotential (1.8 - 2.1 V). Moreover, for electrolysis carried out in the single-cell configuration

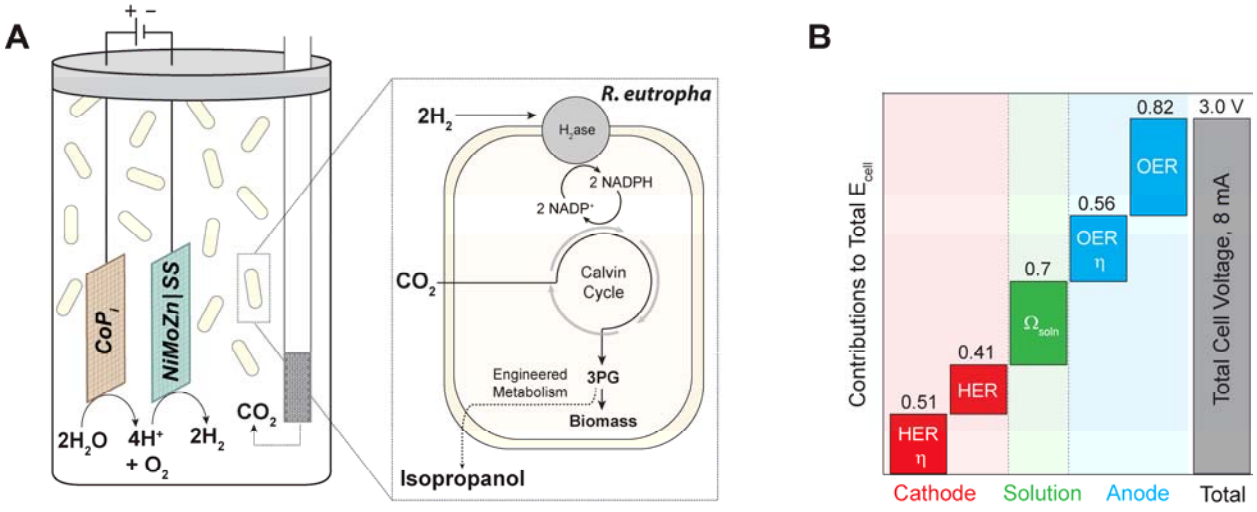

Figure 8 | Schematic diagram of bioelectrochemical cell. A Water oxidation takes place at the cobalt phosphate (CoP_i) anode with proton reduction taking place at the nickel molybdenum zinc (NiMoZn) or stainless steel (SS) cathode. CO_2 is continuously sparged into the cell. The wild-type (wt) bacterium *Ralstonia eutropha (Re)* H16 oxidizes H_2 using oxygen-tolerant hydrogenases (H_2ase) to generate reduced cofactors (e.g. NADPH) and ATP, and uses these to reduce CO_2 to 3-phosphoglycerate (3PG) via the Calvin cycle. 3PG is then converted into biomass in wt *Re*H16, or may be diverted in metabolically engineered *Re*2133-pEG12 into isopropanol. **B** Voltage contributions from CoP_i and NiMoZn water splitting half-reactions, including overpotentials (η), and solution resistance (Ω_{soln}) components for a system driven at E_{cell} = 2.5 V to achieve a current density of ~4 mA/cm^2 (averaged over 5 d).

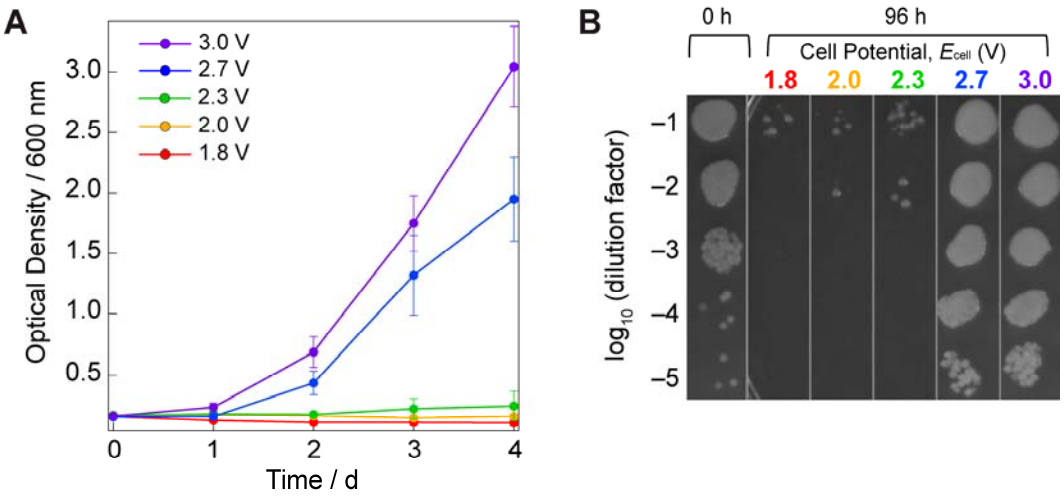

Figure 9 | Cell growth of *R. eutropha*. A Time course of *R. eutropha* cell growth by monitoring optical density at 600 nm, using a CoP_i anode and NiMoZn cathode poised at a range of total cell potentials (E_{cell}); currents obtained at each of these cell potentials. Error bars represent standard error of the mean (S.E.M) with $N = 3 - 5$ independent experiments at each potential. **B** Spot assays of *R. eutropha* prior to starting electrolysis (0 h), or after 96 h of electrolysis with CoP_i/NiMoZn electrodes, as a function of E_{cell}.

of Figure 8A, toxicity is significantly reduced by sparging the cell culture with CO_2 to eliminate excess oxygen (Figure 10B). We also confirmed the production of reactive oxygen species (ROS) at water-splitting underpotentials. Specifically, as shown in Figure 11A, H_2O_2 is detected in the cathode compartment of an H-cell but not in the anode compartment.

The electrolysis experiment was repeated while supplementing the cathodic compartment with 400 µg/mL of an H_2O_2-decomposing enzyme, bovine liver catalase. As shown in Figure 11A, the addition of catalase decreased H_2O_2 to undetectable levels. Catalase addition was sufficient to rescue cell viability at this low E_{cell} (Figure 11B); however, this effect was attenuated for the addition of heat-inactivated catalase. These experiments together establish that enzymatically competent catalase was capable of restoring full cell viability, and furthermore establish a direct link between H_2O_2 availability and cell death, suggesting that cathodically generated H_2O_2 is a major cause of toxicity at low E_{cell}.

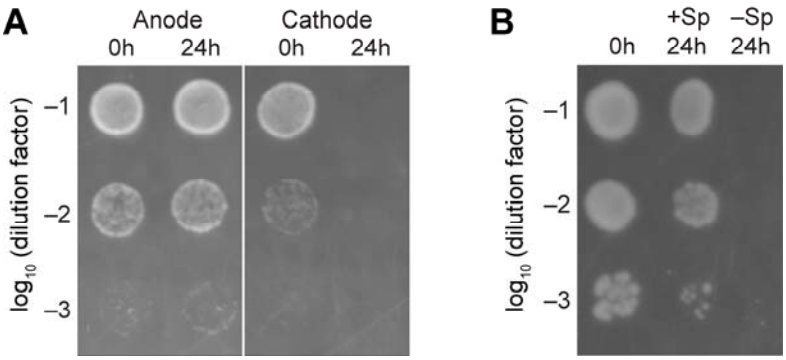

Figure 10 | Spot assays to determine cell toxicity. Spot assays of *R. eutropha* viability following 24 h of electrolysis performed galvanostatically at 0.5 mA/cm^2 (1.8 - 2.1 V) using CoP_i and NiMoZn electrodes: **A** From the cathodic and anodic chambers of an H-cell and **B** from a single cell chamber with (+Sp) and without (–Sp) continuous sparging of CO_2.

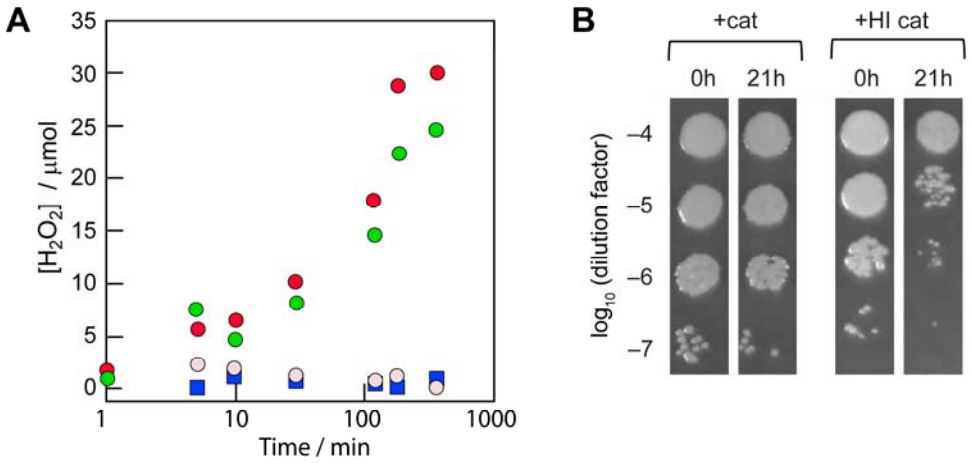

Figure 11 | Effect of catalase on cell viability. A Measurement of H_2O_2 production: in anode (blue squares) and cathode (red circles) of an H-cell subjected to electrolysis performed galvanostatically at 1 mA (E_{cell} = 1.8 - 2.1 V); and, in the cathode with the addition of bovine liver catalase (cat) (gray circles) or heat-inactivated bovine liver catalase (green circles). **B** Accompanying spot assays of *R. eutropha* viability in the cathodic chamber of an H-cell run galvanostatically at 1 mA 1.8 - 2.1 V cell potential with the addition of 400 µg/mL active (+cat) or heat-inactivated (+HI-cat) bovine liver catalase

Wild-type *R. eutropha* H16 was replaced with Re2133-pEG12 in the bioelectrochemical cell shown in Figure 8. The strain produces isopropanol at high yield under fructose-fed, nutrient-limited conditions. As summarized in Figure 12A, whereas wt *R. eutropha* rapidly converts acetyl-CoA to the storage polymer polyhydroxybutyrate (PHB) under nutrient-limited growth conditions, Re2133-pEG12 is disrupted in PHB synthesis and expresses four genes that redirect acetyl-CoA toward the synthesis of isopropanol. Plasmid pEG12 constitutively expresses genes for a ketothiolase (*phaA*) and acetoacetyl-CoA transferase (*ctf*) from *R. eutropha*, and an acetoacetate decarboxylase (*adc*), and alcohol dehydrogenase (*adh*) from *Clostridium sp.* (in red). Both the native *phaA* and a plasmid-encoded copy of phaA (*phaA**) are expressed in this strain, which has also been shown to produce the side products pyruvate and acetone.

Re2133-pEG12 grew robustly in our electrochemical setup and, over the course of 5 d, produced 216 ± 17 mg/L isopropanol (Figure 12B), which was the highest yield of fuel reported for a bioelectrochemical system. Isopropanol production was also highly selective (~90% yield).

The CoP_i OER catalyst permits water splitting to be performed in biologically compatible solutions, and at operating potentials significantly lower than those used in previous bioelectrochemical studies. Specifically, we have shown that the potential used to support biological growth can be decreased by >1.3 V, and that platinum and other rare earth metal electrodes are dispensable.

The ability to achieve bacterial growth at lower potential has revealed a quizzical dependence of biological viability on cell potential at both high ($E_{cell} \geq 4.0$ V) and low ($E_{cell} \leq 2.3$ V) potentials. The loss of cell viability at high potentials has been ascribed logically to the production of ROS via water oxidation at the anode, where oxygen is normally produced in the water splitting reaction. Additionally, it is worth noting that anodic oxidation of chloride to the highly toxic hypochlorite occur at cell potentials of 1.36 V. Although this has long been recognized, it likely contributes to toxicity in recent studies where chloride has been included in the medium.

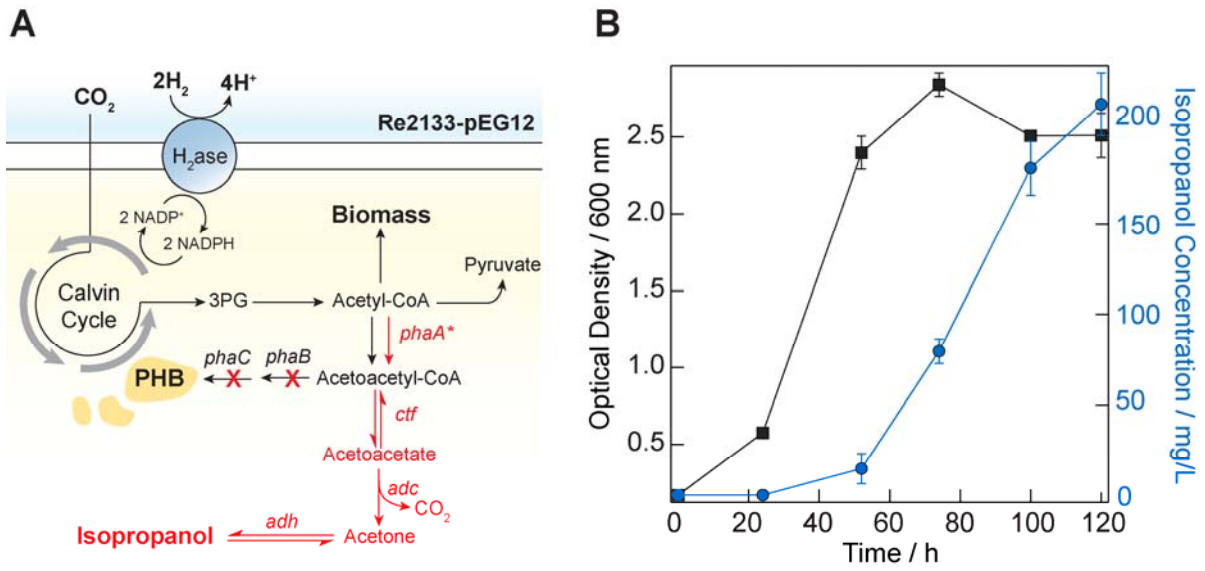

Figure 12 | Bioelectrochemical production of isopropanol. A Schematic diagram of *R. eutropha* strain Re2133-pEG12 containing an engineered pathway for isopropanol production (red lines, text) and grown on electrochemically produced H_2 and CO_2. The CoA transferase (ctf) reaction is reversible and coupled to production of succinyl-CoA from succinate. The alcohol dehydrogenase reaction (adh) is also reversible and coupled to proton transfer and NADPH oxidation (not shown). **B** Growth and isopropanol production in Re2133-pEG12 grown at 3.0 V with a 4 cm^2 CoP_i and 4 cm^2 SS304 anode and cathode, respectively. Error bars represent S.E.M., *N* = 3 independent experiments.

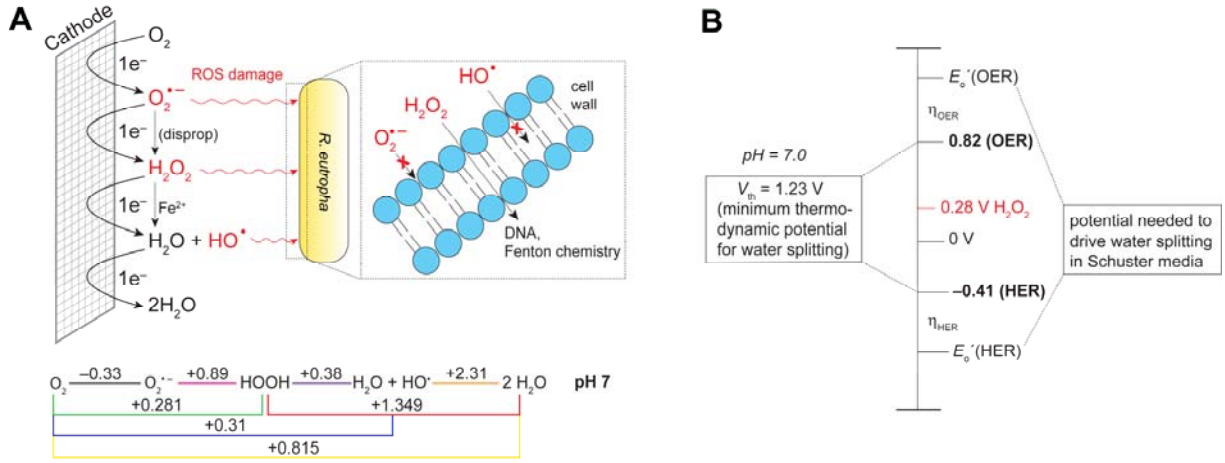

Figure 13 | ROS production. A Schematic of major oxygen reduction reactions at a cathode. The potentials (in volts vs NHE at pH 7.0) for formation of the reactive oxygen species are provided on the Latimer diagram shown in the bottom panel. Generated ROS may cause cell damage at the cell surface or intracellularly (inset). **B** Water splitting potential shown in the context of additional cell potentials and relative to the potential for H_2O_2 generation. The additional potential associated with solution resistance is not shown.

We have shown that the origin of ROS toxicity at the cathode may be understood by considering the Latimer diagram shown in Figure 13A. At pH = 7, the production of superoxide ($O_2^{\bullet-}$), hydrogen peroxide (H_2O_2) and hydroxyl radical ($HO^{\bullet}$) are all thermodynamically favored as compared to the HER couple and thus will be generated at any potential high enough to drive proton reduction. Due to their favorable thermodynamics, ROS production rates will be favored over H_2 production at underpotentials to the water splitting reaction. More generally, lower

potentials will increase the faradaic efficiency of ROS production at the expense of H_2 production. The onset potential of cell growth will be the potential at which H_2 production, which supports cell growth, is sufficient to outweigh the toxic effects of ROS production.

The lower E_{cell} for the CoP_i | NiMoZn or SS water splitting system is manifested in higher overall solar-to-fuels efficiencies. The biomass yields were significantly greater than those previously achieved in integrated bioelectrochemical systems, and the electricity-to-isopropanol yield was the highest solar-to-fuels yield (>300%) observed for an integrated bioelectrochemical system. These increased efficiencies are attributable in part to an increase in the $\eta_{V_{th}}$ term as a result of the ability of the CoP_i catalyst to perform at lower overpotential under bioelectrochemical conditions.

2.2 Bionic Leaf v2.0

The accomplishments of Section 2.1 result in an authentic artificial photosynthetic process (solar light + water + carbon dioxide to biomass and carbon based fuels). However, in undertaking these studies, we discovered that reactive oxygen species (ROS) produced at the cathode were detrimental to cell growth. Because superoxide ($O_2^{\bullet -}$), hydrogen peroxide (H_2O_2) and hydroxyl radical ($HO^{\bullet}$) are all thermodynamically favored as compared to H_2 production at pH = 7, ROS production dominated at potentials at or below the potential to generate H_2. When E_{appl} was at an overpotential that was sufficient to drive water splitting, H_2 production to support cell growth outweighed the toxic effects of ROS. In addition, we found that microbial growth was inhibited due to the leaching of Ni from the NiMoZn alloy into solution. Together, these observations provided an imperative for the development of a biocompatible catalyst system that is not toxic to the bacterium and lowers overpotential for water splitting to translate directly into solar-to-fuel efficiencies that far surpass natural photosynthetic systems.

We turned our efforts to developing a new water splitting catalyst system that derives biocompatibility from a ROS immune cobalt-phosphorus (Co-P) alloy cathode to drive the hydrogen evolution reaction (HER) and from the self-healing properties of the CoP_i anode to drive the oxygen evolution reaction (OER).

The Co-P alloy exhibits high HER activity in water with minimal ROS production. Figure 14A shows that the activity of this Co-P alloy surpasses the activity of the earth-abundant NiMoZn and stainless steel cathodes used in our earlier studies. At constant voltage, a stable HER current is maintained for at least 16 d (Figure 14B). Figure 14C establishes that negligible H_2O_2 is produced during HER, in contrast to that of simple metallic cathodes of Pt and stainless steel (SS).

The Co-P HER and CoP_i OER catalysts work in concert to engender a biocompatible water splitting system. Figure 14D shows the cyclic voltammogram of Co^{2+} in the phosphate buffer (pH = 7). The pre-wave to the catalytic water-splitting current corresponds to the oxidation of Co^{2+} to Co^{3+}, which drives deposition of the catalyst. The CoP_i catalyst exhibits a deposition rate that is linearly proportional to Co^{2+} concentration. The self-healing property of CoP_i is derived from this interplay of the potential at which OER occurs *vs.* the potential at which the catalyst deposits. In concert, the Co-P and CoP_i catalysts preserve extremely low concentrations of Co^{2+} (sub-μM levels) in solution, derived from the self-healing process. This concentration of Co^{2+} is well below the concentration of Co^{2+} (IC_{50} ~ 25 μM) that is toxic to *R. eutropha*. Figure 14E summarizes the chemistry that leads to the biocompatibility of the Co-P|CoP_i water splitting catalyst system. ROS production by Co-P is negligible (pathway 1) and any Co^{2+} that is produced in solution is quickly salvaged by the self-healing process at the CoP_i anode (pathway 2).

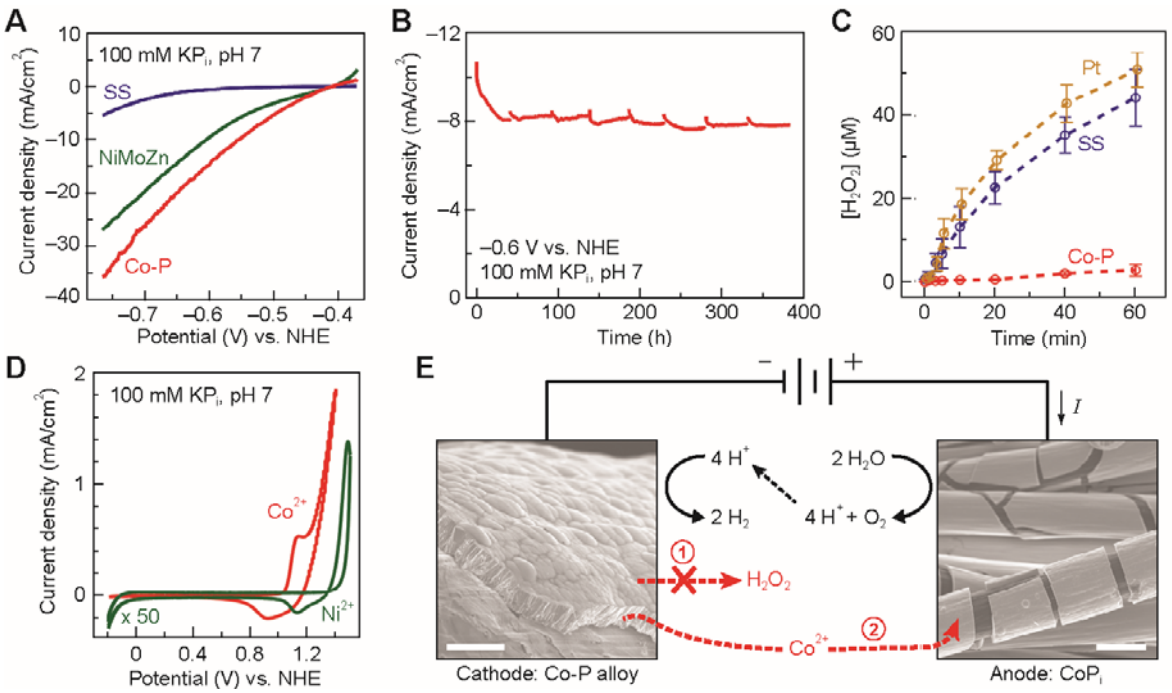

Figure 14 | Active water-splitting catalyst pair with minimal biological toxicity. A. i-V characteristics of different HER catalysts at neutral pH. 10 mV/sec. **B**. 16-d chronoamperometry demonstrates the stability of Co-P cathode at neutral pH. **C**, Abiotic assay of H_2O_2 accumulation for various cathodes combining with CoP_i anode: yellow, Pt; blue, stainless steel (SS); red, Co-P alloy. Device voltage: 2.2 V. n = 3. **D**, Cyclic voltammetry of Co^{2+} and Ni^{2+} in 0.1 M KP_i (pH 7). Metal concentrations are both 0.5 mM, 50 mV/sec. The curves for Ni^{2+} are magnified by 50 times. **E**, Reaction diagram and scanning electron microscopy images for Co-P alloy cathode and CoP_i anode. The main water-splitting reaction is colored in black, and the side reactions that yield toxicants are in red. Scale bars: 10 μm.

Interfacing the biocompatible Co-P|CoP_i electrodes with *R. eutropha* results in an artificial photosynthetic system capable of CO_2-fixation. The CoP_i catalyst was deposited on a high-surface-area carbon cloth as the electrode support (Figure 14E), to result in high currents and a faradaic efficiency of 96±4%. CO_2 reduction proceeded under a constant voltage within a batch reactor. Initial studies were performed under pure CO_2. A known amount of *R. eutropha* was inoculated before water splitting was initiated, and aliquots of solution were withdrawn periodically for chemical analysis. The amount of energy stored through CO_2 reduction was determined by quantifying the accumulation of biomass or specific product of known thermodynamic free energy. By dividing the energy stored from CO_2 reduction with total electrical energy input, the values of η_{elec} were calculated.

The CoP_i | Co-P | *R. eutropha* hybrid system can store over half its input energy as products of CO_2-fixation at low device voltages. A number of driving voltages were tested; as shown in Figure 15A, η_{elec} is generally higher with lower driving voltage. An optimal $\eta_{elec} = 54 \pm 4\%$ was achieved for E_{appl} = 2.0 V over the duration of 6 d. At lower device voltage such as 1.8 V, higher salt concentration is required to facilitate mass transport subsequently high current, but this is undesirable for the metabolism of *R. eutropha* and subsequently η_{elec} suffers (Figure 16A). Enlarging the device by 10-fold in volume did not significantly change the efficiency, indicating that the system is scalable and the reactor volume does not pose immediate limits. Interestingly,

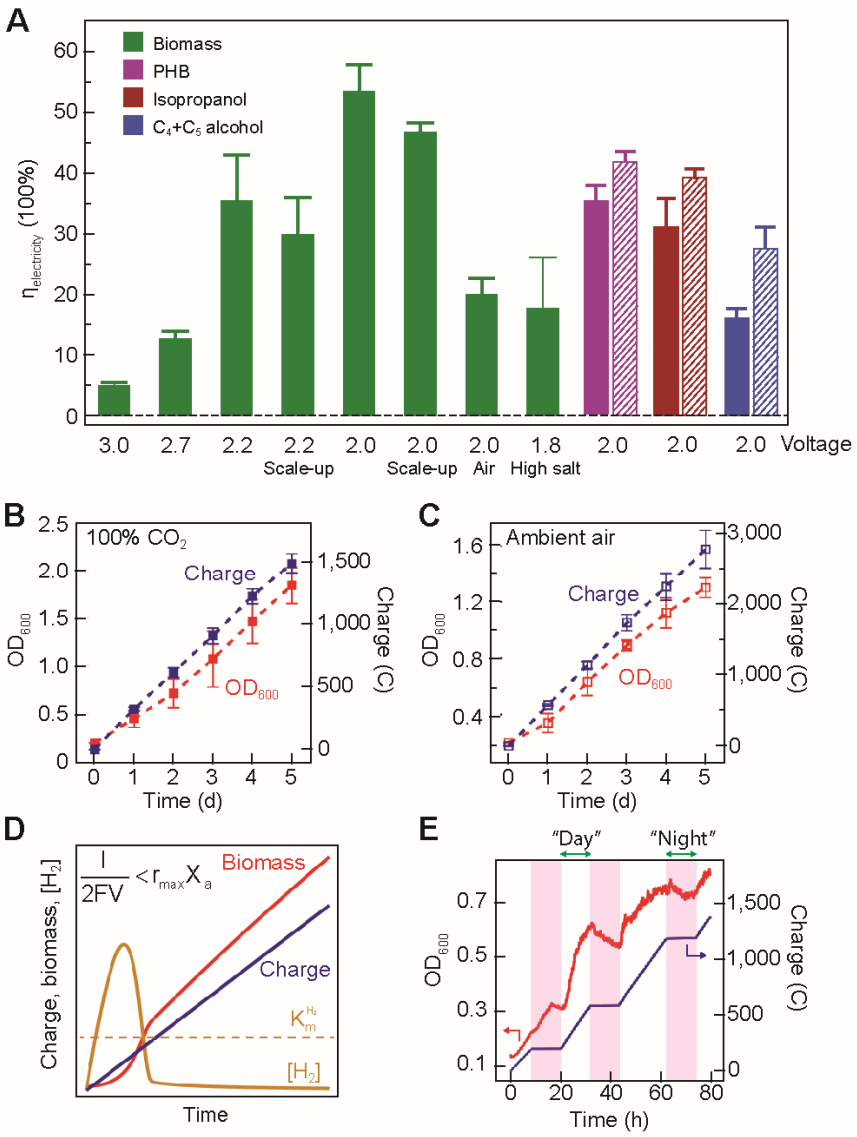

Figure 15 | Energy efficiencies and growth kinetics of hybrid CO_2-reduction device. A, η_{elec} for the production of biomass and chemicals at different driving voltages and various configurations. The solid bars are averages of 5 to 6 days, while the dashed ones are 24-hr maximum. n ≥ 3. **B** & **C**, Under a driving voltage of 2.0 V, the OD_{600}, indictor of biomass accumulation, and the amounts of electric charges that were passed, are plotted *vs.* the duration of experiments with 100% CO_2 (**B**) and air (**C**) in the headspace. **D**, A microbial growth model predicts linear growth. **E**, Real-time monitor of biomass accumulation under "day"/"night" cycle test.

the η_{elec} under air headspace (400 ppm CO_2) is 20 ± 3%, is only 2.7 times lower than the case of pure CO_2 although the partial pressure of CO_2 is reduced by 2,500 times.

Biomass accumulation scales linearly with the amount of charge passed under pure CO_2 (Figure 15B) or ambient CO_2 levels (Figure 15C). The linear growth is accounted for by a model that combines governing equations for H_2-generation from water splitting and biomass accumulation from carbon-fixation. The model predicts a linear correlation between biomass and charge passed after an induction initial period (Figure 15D), which is consistent with observation. Similar linear growth conditions for both pure and ambient CO_2 atmospheres suggest that H_2 oxidation rather

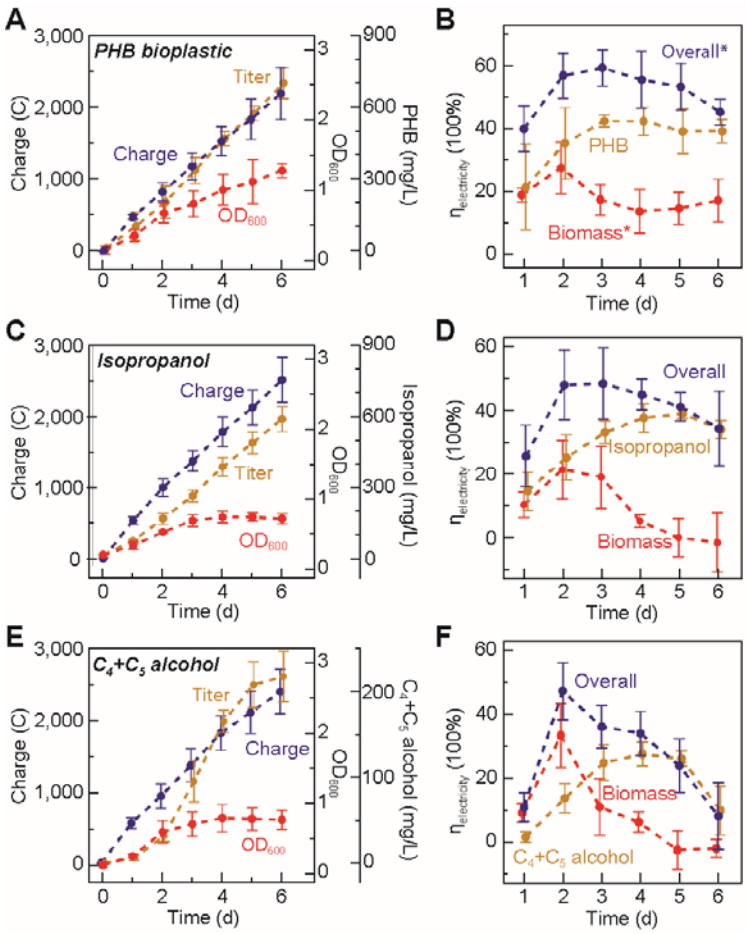

Figure 16 | Efficient synthesis of selective commodity chemicals from CO_2 and water. PHB (**A**, **B**), isopropanol (**C**, **D**), C_4 and C_5 alcohols (**E**, **F**) were selectively produced from the hybrid device. **A**, **C**, and **E**, The OD_{600}, concentrations of selective chemicals, and charges passed through the electrodes are plotted versus the duration of experiments. **B**, **D**, and **F**, The averaged η_{elec} for different products at every intervals of 24 h. The * in **B** indicates that values are possibly over-estimated due to the interference of plastic formation.

than CO_2 reduction is rate limiting for biosynthesis. Lastly, Figure 15E shows the data for a "day"/"night" cycle with real-time biomass monitoring. Microbes halted growth during the "night" session and continued CO_2 reduction 12 hr later, once the water splitting reaction was resumed, confirming the intrinsic dependence of *R. eutropha* on H_2 generation. These data also reveal that the CoP_i | Co-P | *R. eutropha* hybrid system is compatible with the intermittent nature of a solar energy source. Direct CO_2 reduction from air highlights the relatively high affinity of *R. eutropha* for CO_2 at low pressures and at high O_2 concentrations. Given the close coupling of water splitting and microbial growth as well as the subsequent low H_2 concentration in the headspace, our device can potentially capture CO_2 from a fast-flowing air stream without a significant loss of H_2. Such direct CO_2 reduction from air is difficult for an H_2-fed fermenter.

Engineering of *R. eutropha* enables the renewable production of an array of fuel and chemical products. When *R. eutropha* faces nutrient constraints coupled with carbon excess, the biosynthesis of poly(3-hydroxybutyrate) (PHB) is triggered in the wild-type H16 strain. Under a constant rate of water splitting, PHB synthesis was not manifest until nitrogen became limiting (~ day 2),

indicated by the cessation of biomass accumulation (Figure 16A) as well as every 24 hr (Figure 16B). With a titer of ~700 mg/L, the 6-day average for PHB synthesis is η_{elec} = 36 ± 3% with a 24-h maximum of η_{elec} = 42 ± 2% (n = 3) (Figures 15A and 16B). In engineered strains, this PHB pathway can be further modified to produce the fusel alcohols, isopropanol (C_4), isobutanol (C_4), and 3-methyl-1-butanol (C_5) of high energy densities (24, 28, and 31 MJ/L respectively). The accumulation of these liquid fuels follows similar trends as observed for PHB synthesis. Figures 16C and 16D shows that biomass production plateaus while isopropanol titers grow to ~600 mg/L and C_4 + C_5 alcohol titers grow to ~220 mg/L (Figures 16C and 16E). Engineered *R. eutropha* strains produced isopropanol with a 6-d average η_{elec} = 31 ± 4% (Figure 15A) with a 24-h maximum of η_{elec} = 39 ± 2% (Figure 16D); and strains engineered to produce C_4 + C_5 alcohols averaged a 6-d η_{elec} = 16 ± 2% (Figure 15A) with a 24-h maximum of η_{elec} = 27±4 % (Figure 16F). The achieved titers are higher than previous reported values η_{elec} has been increased by at least 20- to 50-fold.

A combined catalyst design mitigates biotoxicity allowing water splitting catalysis to be interfaced to engineered bioorganisms to realize high efficiencies of CO_2 reduction, exceeding that of natural photosynthetic systems. Owing to low driving voltage of 1.8 – 2.0 V for water splitting, high η_{elec} are achieved that translate directly to high solar-to-fuels efficiencies (η_{SFE}) when coupled to typical solar to electricity device ($\eta_{SFE} = \eta_{solar} \times \eta_{elec}$). For a PV of η_{solar} = 18%, the CoP_i | Co-P | *R. eutropha* hybrid system can achieve a η_{SFE} = 9.7% for biomass and 7.8% for fusel alcohols. The system is scalable, providing a platform for the distributed production of solar fuels.

3 Cumulative Personnel

Faculty

Daniel G. Nocera

Postdoctoral Students

Ronny Costi
Chong Liu
Joep J. H. Pjipers

Graduate Students

Kwabena Bediako
Casandra Cox
Christopher Gagliardi
Andrew Ullman
Elizabeth Young

4 Collaborations

Pamela Silver (Harvard Medical School, Harvard University): Bionic leaf

Vladimir Bulović (Department of Electrical Engineering, MIT): Co metal thin films for interface between soft semiconductors and catalyst, for the construction of the artificial leaf

Tonio Buonasissi (Department of Electrical Engineering, MIT): Modelling the artificial leaf and construction of >10% cell.

5 Publications

5.1 Thesis

1. Daniel Kwabena Bediako, Ph.D. 2015, The Electrocatalytic Evolution of Oxygen and Hydrogen by Cobalt and Nickel Compounds
2. Casandra Cox, Ph.D. 2014, Earth-Abundant Water-Splitting Catalysts Coupled to Silicon Solar Cells for Solar-to-Fuels Conversion
3. Andrew Ullman, Ph.D. 2015, Polynuclear Cobalt Complexes as Models of a Cobalt Water Oxidation Catalyst

5.2 Manuscripts

1. "^{13}C-Labeling the Carbon-Fixation Pathway of a Highly Efficient Artificial Photosynthetic System." Liu, C.; Nangle, S. N.; Colón, B. C.; Silver, P. A.; Nocera, D. G, *Faraday Discuss.* **2017**, Ahead of Print, 1–9. DOI: 10.1039/C6FD00231E.
2. "Water Splitting–Biosynthetic System with CO_2 Reduction Efficiencies Exceeding Photosynthesis." Liu, C.; Colón, B. C.; Ziesack M.; Silver. P. A.; Nocera D. G. *Science* **2016**, *352*, 1210–1213.

3. “An Electrochemically Augmented Biosynthetic Platform of CO_2 Fixation.” Liu, C.; Colón, B. C.; Silver, P. A.; Nocera, D. G. *Energy & Fuels*, **2016**, *61*, 148.

4. “Efficient Solar-to-Fuels Production from a Hybrid Microbial | Water Splitting Catalyst System.” Torella J. P.; Gagliardi, C. J.; Chen, J.; Bediako, D. K.; Colón, B. C.; Way, J. C.; Silver, P. A; Nocera D. G. *Proc. Natl. Acad. Sci. U.S.A.* **2015**, *112*, 2337–2342.

5. “Oxygen Evolution Catalysis by Cobalt Oxido Thin Films.” Bediako, D. K.; Ullman, A. M.; Nocera, D. G. *Top. Curr. Chem.* **2015**, *371*, 173–214.

6. “Ten Percent Solar-to-Fuel Conversion with Non-Precious Materials.” Cox, C. R.; Lee, J. Z., Nocera, D. G.; Buonassisi, T. *Proc. Natl. Acad. Sci. U.S.A.* **2014**, *111*, 14057–14061.

7. “Mechanism of Cobalt Self-Exchange Electron Transfer.” Ullman, A. M.; Nocera, D. G. *J. Am. Chem. Soc.* **2013**, *135*, 15053–15061.

8. “Modeling Integrated Photovoltaic-Electrochemical Devices using Steady-State Equivalent Circuits.” Winkler, M. T.; Cox, C, R.; Nocera, D. G.; Buonassisi, T. *Proc. Natl. Acad. Sci. U.S.A.* **2013**, *110*, E1076–1082.

9. “Stabilized CdSe-CoPi Composite Photoanode for Light-Assisted Water Oxidation by Transformation of Thin-Film CdSe/Cobalt Metal.” Costi, R.; Young, E. R.; Bulović V.; Nocera, D. G. *ACS Appl. Mater. Inter.* **2013**, 5, 2364–2367.

10. “Coupling Water-Splitting Catalysts to Silicon Photovoltaics for Direct Solar-to-Fuels conversion.” Cox, C, R.; Winkler, M. T.; Buonassisi, T.; Nocera, D. G. *Energy & Fuels*, **2013**, *58*, 488.

11. “Interfaces Between Water Splitting Catalysts and Buried Silicon Junctions.” Cox, C. R.; Winkler, M. T.; Pijpers, J. J. H.; Buonassisi, T.; Nocera, D.G. *Energy Environ. Sci.* **2013**, *6*, 532–538.

5.3 Patents

1. “Carbon Fixation System and Methods.” Brendan C. Colón, Chong Liu, Marika Ziesack, Pamela Ann Silver and Daniel G. Nocera; September 14, 2016; U.S. Pat. Publ. No. PCT/US2016/051621.

6 Transitions

Science in the AFOSR has been transitioned to the technology sector. Based on research performed under this AFOSR program, two energy storage technologies were created–the artificial leaf for distributed energy storage (in the form of fuels) and by reverse engineering water splitting, a flow battery was created for centralized (i.e. grid) and distributed (i.e. microgrid) energy storage (in the form of electricity). Accordingly, the artificial leaf and flow battery are directly related to each other. On the basis of the above energy storage discoveries, a company Sun Catalytix was founded by the PI. Lockheed Martin purchased the assets of Sun Catalytix in August 2014. The assets were two-fold: (1) the coordination flow battery and (2) the artificial leaf as it pertains to hydrogen management in the flow battery. These energy storage technologies are now being commercialized under the new venture, Lockheed GridStar Flow.

7 Invited Talks

1. MPS Distinguished Lecture; National Science Foundation; Arlington, VA; 14 January 2013.
2. AMN-6: Sixth International Conference on Advanced Materials and Nanotechnology, High School Symposium; Auckland, New Zealand; 13 February 2013.
3. AMN-6: Sixth International Conference on Advanced Materials and Nanotechnology; Auckland, New Zealand; 15 February 2013.
4. Harvard Kennedy School; Harvard University; 4 March 2013.
5. University of California at Berkeley; Department of Chemistry; Berkeley, CA; 8 March 2013.
6. Inaugural Lecture; University of Costa Rica; San Jose, Costa Rica; 12 March 2013.
7. University of Miami; Department of Chemistry; Coral Gables, FL; 29 March 2013.
8. Scripps Institute; Department of Chemistry; San Diego, CA; 3 April 2013.
9. ACS Award Symposium, Inorganic Chemistry Symposium; 245th National ACS Meeting; New Orleans, LA; 7 April 2013.
10. ACS Award Symposium, Organometallic Chemistry; 245th National ACS Meeting; New Orleans, LA; 7 April 2013.
11. The Kavli Foundation Innovations in Chemistry Lecture; 245th National ACS Meeting; New Orleans, LA; 8 April 2013.
12. ACS Symposium, From Benchtop to Business: Energy Solutions for a Green Future; 245th National ACS Meeting; New Orleans, LA; 8 April 2013.
13. ACS Symposium, Heterobimetallic Compounds and their Chemistry; 245th National ACS Meeting; New Orleans, LA; 9 April 2013.
14. Weed Lecture; University of Arizona; Phoenix, AZ; 12 April 2013.
15. Kilpatrick Lecture; Department of Chemistry; Illinois Institute of Technology; 16 April 2013.
16. Jean Dreyfus Boissevain Lecture; Villanova University; Villanova, PA; 24 April 2013.
17. Jean Dreyfus Boissevain Lecture; Villanova University; Villanova, PA; 25 April 2013.
18. Jean Dreyfus Boissevain Lecture; Villanova University; Villanova, PA; 26 April 2013.
19. 2013 Sigma Xi Villanova Research Day Lecture; Villanova University; Villanova, PA; 26 April 2013.
20. Bloch Lecture, University of Chicago; Chicago, IL; 6 May 2013.
21. Tourtellotte Lecture; Kalamazoo College; 9 May 2013.
22. MountainFilm Festival; Telluride, CO; 24 May 2013
23. Science in Japan Forum; Japan Society for the Promotion of Science; Cosmos Club, Washington D.C; 21 June 3013.
24. TEDx; University of Venice; Venice Italy; 30 June 3013.
25. 20th International Symposium on the Photochemistry and Photophysics of Coordination Compounds (ISPPCC); Grand Traverse Resort and Spa; Traverse City, MI; 8 July 2013.

26. GRC Organometallic Chemistry; Salve Regina University; Newport, RI; 11 July 2013.
27. GRC Organic Reactions and Processes; Bryant University; Smithfield, RI; 18 July 2013.
28. 44th World Chemistry Congress of the IUPAC; Istanbul Convention Center; Istanbul, Turkey; 15 August 2013.
29. Solar Energy for World Peace Conference; Istanbul Convention Center; Istanbul, Turkey; 18 August 2013.
30. ISACS 12; Challenges in Chemical Renewable Energy; Cambridge University; Cambridge, England; 4 September 2013.
31. Molecular and Cellular Biology; Harvard University; Woods Hole Marine Biological; Woods Hole, MA: 13 September 2013.
32. CORE Seminar; Michigan State University; East Lansing, MI; 24 September 2013.
33. Huggins Lecturer; Acadia University; Wolfville, Nova Scotia, Canada; 25 September 2013.
34. Department of Chemistry; Acadia University; Wolfville, Nova Scotia, Canada; 26 September 2013.
35. Solvay Lecture; Science for Innovation SFI 13; Brussels, Belgium; 16 October 2013.
36. Chemical and Biomolecular Engineering; Cornel University; Ithaca, NY; 21 September 2013.
37. Oesper Symposium; University of Cincinnati; Cincinnati, OH; 25 October 2013.
38. FAS Campaign Lecture; Harvard University; Cambridge, MA; 26 October 2013.
39. AVS 60th Symposium; American Vacuum Society; Long Beach, CA; 29 October 2013.
40. 2013 Air Force Office of Scientific Research (AFOSR) Bioenergy Meeting; Arlington, VA; 31 October 2013.
41. The Terrawatt Challenge: What Research for our Energy Future?; Accademia Nazionale dei Lincea; Rome, Italy; 6 November 2013.
42. Falling Walls Conference 2013; Berlin, Germany; 9 November 2013.
43. Knights Fellows Lecturer; Cambridge, MA; 12 November 2013.
44. Harvard Club of New York, New York City, NY; 19 November 2013.
45. Public Lecture, Lake Forest, IL; 19 November 2013.
46. Lake Forest Academy; 20 November 2013.
47. Eliot House Tea Lecture, Harvard University, 4 December 2013.
48. NSF CCI Annual Meeting; Huntington Beach, CA; 24 January 2014.
49. Metals in Biology GRC; Ventura, CA; 30 January 2014.
50. Secrataria de Energia, SENER; Mexico City, Mexico; 27 February 2014.
51. National University of Mexico; Mexico City, Mexico; 27 February 2014.
52. Comisión Federal de Electricidad (CFE) of Mexico; Mexico; 28 February 2014.
53. Auburn University, Department of Chemistry; Auburn, AL; 5 March 2014.
54. Kosolapoff Lecturer, Auburn University; Auburn, AL; 6 March 2014.
55. ReConnect, Harvard University; Los Angeles, CA; 8 March 2014.

56. ACS Symposium, Molecular Inorganic Chemistry at the Frontiers of Energy Research; 247th National ACS Meeting; Dallas, TX; 16 March 2014.
57. ACS Award Symposium, Distinguished Service in the Advancement of Inorganic Chemistry: 247th National ACS Meeting; Dallas, TX; 18 March 2014.
58. Harvard University Center for the Environment; Harvard University; Cambridge, MA; 25 March 2014.
59. Weed Lecture; University of Arizona; Tucson, AZ; 27 March 2014.
60. American Physical Society, Northeast Annual meeting; Boston College, Chestnut Hill, MA; 4 April 2014.
61. Warren Lecture, Vanderbilt University; Nashville, TN; 17 April 2014.
62. Big Bang Gala Plenary, California Academy of Science; San Francisco, CA; 24 April 2014.
63. Fahr TomKat Trust; San Francisco, CA; 25 April 2014.
64. University of Kansas; Departments of Chemistry and Chemical Biology; 1 May 2014.
65. Falk-Plaut Lecture, Department of Chemistry; Columbia University; 6 May 2014.
66. Falk-Plaut Lecture, Department of Chemistry; Columbia University; 7 May 2014.
67. Stauffer Lecture, Department of Chemistry; Columbia University; 19 May 2014.
68. Stauffer Lecture, Department of Chemistry; Columbia University; 21 May 2014.
69. University of Crete; Heraklion, Crete, Greece; 27 May 2014.
70. 36th DOE Solar Photochemistry Meeting; Annapolis, MD; 4 June 2014.
71. 3rd International Workshop on Solar Energy for Sustainability; Nanyang Technical University; Singapore; 11 June 2014.
72. PCET 2014: Second International Conference on Proton-Coupled Electron Transfer; Skokloster Wärdshus, Sweden; 18 June 2014.
73. ICPP-8; Istanbul, Turkey; 26 June 2014.
74. Materials for Solar-Driven Fuels Synthesis, University College London; London, UK; 7 July 2014.
75. Theo Murphy Scientific Discussion Meeting; Kavli Royal Society Centre; Chicheley, England; 8 July 2014.
76. GRC Electron Donor-Acceptor; Newport, RI; 8 August 2014.
77. ACS Presidential Symposium; 248th National ACS Meeting; San Francisco, CA; 12 August 2014.
78. DARPA Biological Technologies Office; Arlington, VA; 22 August 2014.
79. National Renewable Energy Laboratory; Golden, CO; 26 August 2014.
80. 2014 Air Force Office of Scientific Research (AFOSR) Bioenergy Meeting; Arlington, VA; 8 September 2014.
81. MSU Green Lecture; Michigan State University, East Lansing, MI; 16 September 2014.
82. Apple; Cupertino, CA; 19 September 2014.
83. Office of the President; Harvard University; 21 September 2014.

84. Jacob Bigeleisen Lecture, Stony Brook University, Stony Brook, NY; 26 September 2014
85. Department of Chemistry; Texas A&M University; College Station, TX; 1 October 2014.
86. Robert Bosch GmbH; Cambridge, MA; 17 October 2014.
87. Harvard Your Texas; Dallas, TX; 25 October 2014.
88. Class of '42 Lecture, Bridgewater State University, Bridgewater, MA; 28 October 2014.
89. Green Buildings and Cities; Graduate School of Design; Harvard University; 7 November 2014.
90. Wright Lecture; Wright Foundation; Geneva, Switzerland; 14 November 2014.
91. International Conference on Artificial Photosynthesis; Awaji City, Hyogo, Japan; 24 November 2014.
92. Royal Australian Chemical Institute National Congress; Adelaide, Australia, 12 December 2014.
93. Frontiers in Chemistry Lecture, Department of Chemistry, Wayne State University; 16 January 2015
94. CCI, National Science Foundation; Newport Beach, CA; 25 January 2015
95. Graduate School of Design; Harvard University; Cambridge, MA; 6 February 2015.
96. Distinguished Lecture, School of Science, Hong Kong Polytechnic University; Hong Kong, China; 16 February 2015.
97. McGregory Lecture, Colgate University; Hamilton, NY; 20 February 2015.
98. Department of Biochemistry; University of Illinois Urbana-Champaign; Urbana, IL; 27 February 2015.
99. ACS Award Symposium, Distinguished Service in the Advancement of Inorganic Chemistry: 249th National ACS Meeting; Denver, CO; 23 March 2015.
100. Precursory Research for Embryonic Science and Technology (PRESTO) Keynote Lecture; Tokyo, Japan; 26 March 2015.
101. Symposium on Next Generation Electrochemical Energy Storage and Conversion Systems; 2015 Spring MRS Meeting; 9 April 2015.
102. Graduate School of Arts and Sciences; Harvard University; Cambridge, MA; 11 April 2015.
103. Jean Dreyfus Boissevain Lecture; Ithaca College; Ithaca, NY; 16 April 2015.
104. Jean Dreyfus Boissevain Lecture; Ithaca College; Ithaca, NY; 17 April 2015.
105. Real Estate Academic Initiative; Harvard University; Cambridge, MA; 23 April 2015.
106. 1st International Solar Fuels Conference; Uppsala, Sweden; 28 April 2015.
107. Public Lecture; Uppsala, Sweden; 29 April 2015.
108. Anthony J. and Heand Johns Silvestri Lectureship in Chemistry; Villanova University; Villanova, PA; 1 May 2015.
109. Institut de France; Académie des Sciences; Paris France; 5 May 2015.
110. Hybrid Organic Photovoltaics-15 (HOPV-15); Rome, Italy; Rome; 12 May 2015.
111. Graduate Student Symposium; University of Buffalo; Buffalo, NY; 18 May 2015.

112. Department of Chemistry; Michigan State University; East Lansing, MI; 19 May 2015.
113. 37th DOE Solar Photochemistry Meeting; Gaithersburg, MD; 3 June 2015.
114. America Answers: Future of Energy; Studio Theatre; Washington Post; Washington, D.C.; 23 June 2015.
115. 27th International Conference on Photochemistry (ICP2015); Jeju Island, Korea; 30 June 2015.
116. SFN International Discussion Meeting: Solar Fuels: Moving from Materials to Devices; The Royal Society; London, England; 8 July 2015.
117. Barber Symposium; Imperial College London; London, England; 9 July 2015.
118. 5th Asian Conference on Coordination Chemistry; Hong Kong, China; 13 July 2015.
119. 12th International Conference on Materials Chemistry (MC12); The Royal Society of Chemistry; University of York; York, England; 20 July 2015.
120. Inorganic Chemistry Lectureship Symposium; 250th ACS National Meeting; Boston, MA; 17 August 2015.
121. ACS Office of Public Affairs Symposium, The Public Perception of the Chemistry Enterprise; 250th ACS National Meeting; Boston, MA; 17 August 2015.
122. ACS Symposium, Innovative Chemistry & Electrocatalysis for Low-Carbon Energy & Fuels: Discovery to Application Symposium; 250th ACS National Meeting; Boston, MA; 18 August 2015.
123. GSSPC Symposium: Academic Innovations for Tomorrow's Industries; 250th ACS National Meeting; Boston, MA; 18 August 2015.
124. ACS Symposium, High-Energy Organometallic Complexes: Reactivity Driving New Synthesis and Catalysis; 250th ACS National Meeting; Boston, MA; 18 August 2015.
125. Banque Cantonale de Genève; Geneva, Switzerland; 4 September 2015.
126. ISACS 17; Challenges in Chemical Renewable Energy; Rio de Janeiro, Brazil; 9 September 2015.
127. Faraday Discussion on Supramolecular Chemistry; The Royal Society of Chemistry; Cambridge, England; 16 September 2015.
128. Christian Doppler Symposium on Solar Fuels; University of Cambridge; Cambridge, England; 18 September 2015.
129. Knights Fellows Lecturer; MIT; Cambridge, MA; 29 September 2015.
130. Harvard University Climate Change Symposium; Harvard University; Cambridge, MA; 1 October 2015.
131. Artificial Photosynthesis; Innovation for Cool Earth Forum (ICEF); Secretariat of ICEF and Director, Ministry of Economy, Trade and Industry; Tokyo, Japan; 8 October 2015.
132. ICEF Energy Storage Roadmap; Secretariat of ICEF and Director, Ministry of Economy, Trade and Industry; Japan; 8 October 2015.
133. MSU Green Lecture; Michigan State University, East Lansing, MI; 20 October 2015.
134. UN 70th Anniversary Gala Celebration Sustainably Lighting the World; United Nations Foundation, East Lansing, MI; 25 October 2015.

135. 2015 Air Force Office of Scientific Research (AFOSR) Bioenergy Meeting; San Antonio, TX; 2 November 2015.
136. Harvard TEDx; Harvard University; Cambridge, MA; 7 November 2015.
137. Science Research Lecture; Science Center Harvard University; Cambridge, MA; 18 November 2015.
138. Harvard Club of Cape Cod; Hyannis, MA; 19 October 2015.
139. Bioinspired Solar Energy; Canadian Institute for Advanced Research (CIFAR); San Francisco, CA; 12 December 2015.
140. Symposium on Photocatalysis and Charge Transfer at Interfaces and Nanomaterials; The International Chemical Congress of Pacific Basins Societies; Honolulu, HI; 17 December 2015.
141. GRC Metals in Biology; Ventura, CA; 27 January 2016.
142. Torkil Holm Symposium; Danish Academy of Sciences; Copenhagen, Denmark; 29 January 2016.
143. Department of Chemistry; Princeton University; Princeton, NJ; 11 February 2016.
144. Public Lecture; Tulane University; New Orleans, LA; 14 February 2016.
145. Jonassen Lecture; Tulane University; New Orleans, LA; 15 February 2016.
146. GRC Solar Fuels; Lucca Italy; 3 March 2016.
147. Leigh Ann Conn Lecture, University of Louisville, Louisville, KY; 9 March 2016.
148. ACS Award Symposium, Inorganic Chemistry; 251st National ACS Meeting; San Diego, CA; 13 March 2016.
149. ExxonMobil Award Symposium, Solid State Chemistry Faculty Fellow Award; 251st National ACS Meeting; San Diego, CA; 13 March 2016.
150. ACS Award Symposium, F. Albert Cotton Award in Synthetic Inorganic Chemistry; 251st National ACS Meeting; San Diego, CA; 14 March 2016.
151. ACS Symposium, Computational Chemistry Across Catalysis From Metallic Nanoparticles to Isolated Metal Active Site; 251st National ACS Meeting; San Diego, CA; 15 March 2016.
152. 4th International Workshop on Solar Energy for Sustainability "Photosynthesis and Bioenergetics"; Nanyang Technological University; Singapore; 21 March 2016.
153. Department of Chemistry; University of Massachusetts Amherst; Amherst, MA; 31 March 2016.
154. 5th SolarTech International Conference; Munich, Germany; 6 April 2016.
155. Institute of Molecular Engineering; University of Chicago; Chicago, IL; 14 April 2016.
156. MLH Green Lectureship; Inorganic Chemistry Laboratory; Oxford University; Oxford United Kingdom; 20 April 2016.
157. Department of Economics; University of Chicago; Chicago, IL; 18 May 2016.
158. School of Chemistry, University of St. Andrews, St. Andrews, Scotland, 30 May 2016.
159. School of Chemistry, University of Edinburgh, Edinburgh Scotland, 31 May 2016.
160. Institute of Chemical Sciences at Heriot-Watt, Edinburgh Scotland, 1 June 2016.

161. Robert Black Lecture, School of Chemistry, University of Glasgow, Glasgow Scotland, 2 June 2016.
162. Department of Pure and Applied Chemistry, University of Strathclyde, Glasgow Scotland, 3 June 2016.
163. GRC Metallocofactors; Stonehill College, Easton, MA; 13 June 2016.
164. 9th European Meeting on Solar Chemistry and Photocatalysis: Environmental Applications; Strasbourg, France; 16 June 2016.
165. 20th International Symposium on Homogeneous Catalysis; Kyoto, Japan; 15 July 2016.
166. 17th International Congress on Photosynthesis Research; Maastricht, Netherlands; 9 August 2016.
167. Gordon Goodman Lecture, Royal Swedish Academy of Sciences and the Stockholm Environment Institute, 15 September 2016.
168. Frontiers in Chemistry Lecturer; Department of Chemistry; Case Western University Cleveland, OH; 29 September 2016.
169. Evans Lecture; Department of Chemistry, Ohio State University; Columbus, OH; 6 October 2016.
170. Evans Lecture; Department of Chemistry, Ohio State University; Columbus, OH; 7 October 2016.
171. Lind Lecture; Department of Chemistry, University of Tennessee; Knoxville, TN; 13 October 2016.
172. Evans Lecture; Oak Ridge National Laboratory; Knoxville, TN; 14 October 2016.
173. MSU Green Lecture; Michigan State University, East Lansing, MI; 18 October 2016.
174. 2016 Air Force Office of Scientific Research (AFOSR) Bioenergy Meeting; Dayton, OH; 1 November 2016.
175. Axalta Lecture, University of Pennsylvania, Philadelphia, PA; 4 November 2016.
176. iCONS Lecture; University of Massachusetts, Amherst, MA; 8 November 2016.
177. Harvard Global Initiative, Symposium: Climate Change and the Developing World; Harvard University, Cambridge, MA; 16 November 2016.
178. Knight Fellows Lecturer; MIT, Cambridge, MA; 22 November 2016.
179. 2016 Annual Meeting of the Chinese Chemical Society; National Chung Hsing University, Taichung, Taiwan; 4 December 2016.
180. Institute of Chemistry, Academia Sinica, Taipei, Taiwan; 5 December 2016.
181. Department of Chemistry; National Taiwan Normal University, Taipei, Taiwan; 6 December 2016.
182. P. B. Ray Lecture, Symposium on Advanced Biological Inorganic Chemistry (SABIC-2017); Kolkata, India; 9 January 2017.
183. Shri V.V. Mariwala Lecture; Institute of Chemical Technology, Mumbai, India; 13 January 2017.
184. Director's Lectureship; Argonne National Laboratory, Argonne, IL 26 January 2017.

185. Winston Ko Lecture; University of California at Davis, Davis. CA; 9 February 2017.
186. Department of Chemistry; University of California at Davis, Davis. CA; 10 February 2017.
187. Hawthorne Lecture; Department of Chemistry, UCLA, Westwood, CA; 22 February 2017.
188. Distinguished Lecturer in Chemistry; University of Texas at Dallas, Dallas, TX; 23 February 2017.
189. Department of Chemistry, University of Texas at Dallas, Dallas, TX; 24 February 2017.
190. Faraday Discussion, Artificial Photosynthesis; Kyoto, Japan; 2 March 2017.
191. International Conference on Artificial Photosynthesis (ICARP2017); Ritsumeikan University; Kyoto, Japan; 3 March 2017.
192. The Academy Lecture, Royal Swedish Academy of Sciences; Stockholm, Sweden; 8 March 2017.

8. Honors

8.1 Awards

1. Leigh Ann Conn Prize in Renewable Energy, 2016
2. Fellow, Royal Society of Chemistry, 2015
3. Honorary Degree, Doctorate of Science, University of Crete, 2014
4. ACS Kosolapoff Award, 2014
5. Indian Academy of Sciences, 2013
6. Honorary Degree, Master of Arts, Harvard University, 2013
7. Jury Prize, Sundance Film Festival, 2013

8.2 Honorary Lectureships

1. The Academy Lecture, Royal Swedish Academy of Sciences, 2017
2. CSA Distinguished Lecture, University of Texas at Dallas, 2017
3. Hawthorne Lecture, UCLA, 2107
4. Winston Ko Lecture, University of California at Davis, 2017
5. Director's Lectureship, Argonne National Laboratory, 2017
6. P.B. Ray Lecture, Kolkata, India, 2017
7. Shri V. V. Mariwala Lectureship, Institute of Chemical Technology Mumbai, India, 2017
8. 113 Axalta Lectureship, University of Pennsylvania, 2016
9. Lind Lectures, Oak Ridge National Laboratory and University of Tennessee, 2016
10. Evans Lectures, Ohio State University, 2016
11. Frontiers in Chemistry Lecture, Case Western University, 2016
12. Gordon Goodman Lecture, Royal Academy of Sciences, 2016
13. ScotChem Lectures, Scotland, 2016
14. Robert Black Lecture, Glasgow University, 2016

15. MLH Green Lecture, Oxford University, 2016
16. Leigh Ann Conn Prize Lecture, University of Louisville, 2016
17. Jonassen Lecture, Tulane University, 2016
18. Silvestri Lecture, Villanova University, 2015
19. Jean Dreyfus Boissevain Lectures, Ithaca College, 2015
20. McGregory Lecture, Colgate University, 2015
21. School of Science Distinguished Lecture, Hong Kong Polytechnic University, 2015
22. Frontiers in Chemistry Lecture, Wayne State University, 2015
23. Jacob Bigeleisen Lecture, Stony Brook University, 2014
24. Class of '42 Lecture, Bridgewater State University, 2014
25. Stauffer Lectures, Stanford University, 2014
26. Falk-Plaut Lectures, Columbia University, 2014
27. Warren Lecturer, Vanderbilt University, 2014
28. Weed Lecturer, University of Arizona, 2014
29. Kosolapoff Lecturer, Auburn University, 2014
30. Tourtelotte Lecturer, Kalamazoo College, 2013
31. Bloch Lecturer, University of Chicago, 2013
32. Huggins Lecturer; Acadia University, 2013
33. Solvay Lecture, Solvay, Brussels, 2013
34. Sigma Xi Villanova Research Day Lecture, Villanova University, 2013
35. Jean Dreyfus Boissevain Lectures, Villanova University, 2013
36. Kilpatrick Lecture, Illinois Institute of Technology, 2013
37. Kavli Innovation Lecture, American Chemical Society, 2013
38. Inaugural Lecture; University of Costa Rica, 2013
39. MPS Distinguished Lecture, National Science Foundation, 2013

AFOSR Deliverables Submission Survey

Response ID:7708 Data

1.

Report Type

Final Report

Primary Contact Email

Contact email if there is a problem with the report.

dnocera@fas.harvard.edu

Primary Contact Phone Number

Contact phone number if there is a problem with the report

617-495-8904

Organization / Institution name

Harvard University

Grant/Contract Title

The full title of the funded effort.

Catalysts for Lightweight Solar Fuels Generation

Grant/Contract Number

AFOSR assigned control number. It must begin with "FA9550" or "F49620" or "FA2386".

FA9550–13–1–00289

Principal Investigator Name

The full name of the principal investigator on the grant or contract.

Daniel G. Nocera

Program Officer

The AFOSR Program Officer currently assigned to the award

Patrick O. Bradshaw

Reporting Period Start Date

02/01/2013

Reporting Period End Date

01/31/2017

Abstract

The artificial leaf was created to provide a simple mechanism for the storage of solar energy in the form of the chemical fuels of hydrogen and oxygen, produced from solar water splitting. The artificial leaf comprises a single crystalline Si coated with a NiMoZn or Co-P alloy as the hydrogen evolution catalyst and cobalt phosphate (CoPi) or nickel borate (NiBi) as the oxygen evolution catalyst. Modeling this buried junction architecture provided a rational framework for the design and construction of devices with solar-to-hydrogen efficiencies greater than 10%. The concept of solar fuels was advanced by coupling the functional componentry of the artificial leaf with the H2-oxidizing bacteria, Ralstonia eutropha. In this body of work, R. eutropha is used to efficiently convert CO2, along with H2 produced from water splitting catalysts of the artificial leaf, into biomass and fusel alcohols. In this integrated setup, equivalent solar-to-biomass yields of up to 10.2% and solar-to-liquid fuel (e.g., fusel alcohols) yields of 5-7% have been achieved. These yields greatly exceed natural photosynthetic systems of crops

(1%) and microalgae (3%). This scalable system scrubs a CO2 equivalent of about 230,000 liters of air per kWh of electricity. The work provides a distributed method to store solar energy in the form of fuels.

Distribution Statement
This is block 12 on the SF298 form.

Distribution A - Approved for Public Release

Explanation for Distribution Statement
If this is not approved for public release, please provide a short explanation. E.g., contains proprietary information.

SF298 Form
Please attach your SF298 form. A blank SF298 can be found here. Please do not password protect or secure the PDF The maximum file size for an SF298 is 50MB.

sf0298_completed.pdf

Upload the Report Document. File must be a PDF. Please do not password protect or secure the PDF . The maximum file size for the Report Document is 50MB.

AFOSR7_Final_Report_v2.pdf

Upload a Report Document, if any. The maximum file size for the Report Document is 50MB.

Archival Publications (published) during reporting period:

Thesis
1. Daniel Kwabena Bediako, Ph.D. 2015, The Electrocatalytic Evolution of Oxygen and Hydrogen by Cobalt and Nickel Compounds
2. Casandra Cox, Ph.D. 2014, Earth-Abundant Water-Splitting Catalysts Coupled to Silicon Solar Cells for Solar-to-Fuels Conversion
3. Andrew Ullman, Ph.D. 2015, Polynuclear Cobalt Complexes as Models of a Cobalt Water Oxidation Catalyst

Manuscripts
1. "13C-Labeling the Carbon-Fixation Pathway of a Highly Efficient Artificial Photosynthetic System." Liu, C.; Nangle, S. N.; Colón, B. C.; Silver, P. A.; Nocera, D. G, Faraday Discuss. 2017, Ahead of Print, 1–9. DOI: 10.1039/C6FD00231E.
2. "Water Splitting–Biosynthetic System with CO2 Reduction Efficiencies Exceeding Photosynthesis." Liu, C.; Colón, B. C.; Ziesack M.; Silver. P. A.; Nocera D. G. Science 2016, 352, 1210–1213.
3. "An Electrochemically Augmented Biosynthetic Platform of CO2 Fixation." Liu, C.; Colón, B. C.; Silver, P. A.; Nocera, D. G. Energy & Fuels, 2016, 61, 148.
4. "Efficient Solar-to-Fuels Production from a Hybrid Microbial | Water Splitting Catalyst System." Torella J. P.; Gagliardi, C. J.; Chen, J.; Bediako, D. K.; Colón, B. C.; Way, J. C.; Silver, P. A; Nocera D. G. Proc. Natl. Acad. Sci. U.S.A. 2015, 112, 2337–2342.
5. "Oxygen Evolution Catalysis by Cobalt Oxido Thin Films." Bediako, D. K.; Ullman, A. M.; Nocera, D. G. Top. Curr. Chem. 2015, 371, 173–214.
6. "Ten Percent Solar-to-Fuel Conversion with Non-Precious Materials." Cox, C. R.; Lee, J. Z., Nocera, D. G.; Buonassisi, T. Proc. Natl. Acad. Sci. U.S.A. 2014, 111, 14057–14061.
7. "Mechanism of Cobalt Self-Exchange Electron Transfer." Ullman, A. M.; Nocera, D. G. J. Am. Chem. Soc. 2013, 135, 15053–15061.
8. "Modeling Integrated Photovoltaic-Electrochemical Devices using Steady-State Equivalent Circuits." Winkler, M. T.; Cox, C, R.; Nocera, D. G.; Buonassisi, T. Proc. Natl. Acad. Sci. U.S.A. 2013, 110, E1076–1082.
9. "Stabilized CdSe-CoPi Composite Photoanode for Light-Assisted Water Oxidation by Transformation of Thin-Film CdSe/Cobalt Metal." Costi, R.; Young, E. R.; Bulović V.; Nocera, D. G. ACS Appl. Mater. Inter. 2013, 5, 2364–2367.
10. "Coupling Water-Splitting Catalysts to Silicon Photovoltaics for Direct Solar-to-Fuels conversion." Cox, C, R.; Winkler, M. T.; Buonassisi, T.; Nocera, D. G. Energy & Fuels, 2013, 58, 488.
11. "Interfaces Between Water Splitting Catalysts and Buried Silicon Junctions." Cox, C. R.; Winkler, M. T.; Pijpers, J. J. H.; Buonassisi, T.; Nocera, D.G. Energy Environ. Sci. 2013, 6, 532–538.

Patents

1. "Carbon Fixation System and Methods." Brendan C. Colón, Chong Liu, Marika Ziesack, Pamela Ann Silver and Daniel G. Nocera; September 14, 2016; U.S. Pat. Publ. No. PCT/US2016/051621.

New discoveries, inventions, or patent disclosures:

Do you have any discoveries, inventions, or patent disclosures to report for this period?

Yes

Please describe and include any notable dates

The bionic leaf: "Carbon Fixation System and Methods." Brendan C. Colón, Chong Liu, Marika Ziesack, Pamela Ann Silver and Daniel G. Nocera; September 14, 2016; U.S. Pat. Publ. No. PCT/US2016/051621.

Do you plan to pursue a claim for personal or organizational intellectual property?

Yes

Changes in research objectives (if any):

No change

Change in AFOSR Program Officer, if any:

No change

Extensions granted or milestones slipped, if any:

NA

AFOSR LRIR Number

LRIR Title

Reporting Period

Laboratory Task Manager

Program Officer

Research Objectives

Technical Summary

Funding Summary by Cost Category (by FY, $K)

	Starting FY	FY+1	FY+2
Salary			
Equipment/Facilities			
Supplies			
Total			

Report Document

Report Document - Text Analysis

Report Document - Text Analysis

Appendix Documents

2. Thank You

E-mail user

Mar 10, 2017 15:53:07 Success: Email Sent to: dnocera@fas.harvard.edu